Characterisation of Raw and Recovered Electronic Waste Metal Oxides from Computer Village, Ogbunabali, Port Harcourt, Nigeria

Gbarakoro, S. L., Konne, J. L., Boisa, N. and Bull, O. S.
Department of Chemistry, Rivers State University,
Nkpolu-Oroworukwo, Port Harcourt, Nigeria

D.O.I: 10.56201/ijccp.v10.no1.2024.pg22.60

Abstract

*Electronic wastes such as batteries, cell phones, laptops, radios and televisions obtained from electronic shops and dumpsites in Port Harcourt, Nigeria were dismantled, crushed, incinerated, pulverized, sieved and extracted. The powdered and dried e-waste samples as well as metal oxides found in both raw and recovered e-wastes were characterized using appropriate methods. The XRD patterns showed the major mineral phases as quartz, alumina, alumina, calcite, quartz, quartz, quartz, cassiterite, quartz and quartz for raw samples respectively and halite, vallerite, manganite, thenardite, calcium hydroxide, chalcopyrite, gibbsite, sylvine sodian, and gibbsite for recovered samples respectively. The SEM micrographs demonstrated noticeable morphological differences among the samples. The surface morphology also showed smaller particle sizes as well as large particle sizes of 20µm. The results of FTIR confirmed the finger print regions of the major mineral phases. The EDXRD analysis for composition of metal oxides showed SnO_2 (5.30%), Al_2O_3, (27.87%), Al_2O_3, (14.22 %), CaO (23.41 %), CuO (52.47 %), Fe_2O_3 (14.31 %), Co_3O_4 (56.37 %), SnO_2 (11.44 %), Co_3O_4 (7.74 %) and Fe_2O_3 (17.12 %) as the highest metal oxides for raw samples and Al_2O_3, (10.85 %), Fe_2O_3 (26.96 %), CuO (66.89 %), CaO (17.39 %), Co_3O_4 (26.70 %), Co_3O_4 (45.77 %), Fe_2O_3 (10.39 %), Al_2O_3, (63.67 %), MgO (4.92 %), and Al_2O_3 (29.68 %), as the highest metal oxides for recovered samples .Some metal oxides that were found in the raw components were found to be absent or non-crystalline in the recovered compounds. The characterization of e-waste components could be conducted in order to reveal the correlation between toxic substances in e-waste and recovery (treatment) strategies***.***

Keywords*: Characterisation, Metal Oxides, E-waste, XRD, EDXRF*

1.0 Introduction

Electronic waste includes all components, sub-assemblies and consumables, which are part of the product at the time of discarding (Khaliq *et al*., 2014). Discarded electronic products such as mobile phones, batteries, radios, televisions, musical instrument, type-writers, computers, calculators, refrigerators, washing machines, clocks and watches are categorized under e-waste. E-waste is also viewed by Khaliq *et al*., (2014) as a complex mixture comprising of ferrous, nonferrous, plastic and ceramic materials. Ewuim *et al*., (2014) classified non-ferrous metals to include aluminium, copper, platinum, silver and gold. Magalini *et al*., (2015) also listed europium (Eu) and terbium (Tb) as scarce and valuable resources embedded in e-waste. These valuable metals in the resource content of discarded e-waste are 40-50 times richer than natural deposits (Abalansa *et al*., 2021). Some of the toxic components present in discarded e-waste as reported in the literature include heavy metals such as cadmium (Cd), cobalt (Co), chromium (Cr), lead (Pb), nickel (Ni), and copper (Cu), iron (Fe), lithium (Li), barium (Ba), beryllium (Be), lanthanum (La), mercury (Hg), manganese (Mn), molybdenum (Mo), silver (Ag), gold (Au) as well as persistent organic pollutants (POPs), such as dioxin, brominated flame retardants (BFRs) (Borthakur, 2016),

hexavalent chromium (Cr(VI)), polycyclic aromatic hydrocarbons (PAHs), polychlorinated biphenyls (PCBs), polybrominated dibenzo-p-dioxins and dibenzofurans (PBDD/Fs), polychlorinated dibenzo-p-dioxins and dibenzofurans (PCDD/Fs) and polyvinyl chloride (PVC) (Yunus and Sengupta, 2016). The presence of these metals and compounds makes e-waste to be considered as a hazardous material (Pant *et al*., 2012). These metals can be mixed or alloyed with some other metal or non-metal in order to enhance their mechanical or chemical properties. Some of these alloys are applicable in the manufacture of electronic appliances including musical instruments, battery caps, condenser tubes and valves (Debnath *et al*., 2016; Isildar *et al*., 2019).

The production of e-waste worldwide is increasing tremendously and is expected to skyrocket far beyond human imagination. Based on recent researches, e-waste which is a fraction of municipal waste is growing very fast and large in the near future (Ongondo *et al*., 2011; Isildar *et al*., 2019). At present, 20 to 25 million tons per year of e-waste are being generated globally with Europe, United States of America (USA) and Australia taking the lead (Khaliq *et al*., 2014). Robinson (2009) listed China, Eastern Europe and Latin America as countries expected to become significant e-waste producers in the next decade. The production of e-waste in Europe is also expected to increase by 45 % between 1995 and 2020 (Khaliq *et al*., 2014). According to Davis and Heart (2008); Yunus and Sengupta (2016); Wang *et al*., (2016), 20-50 million tonnes of e-waste are generated globally every year. Isildar *et al*., 2019 reported that e-waste had reached a global total of 41.8 million tons per annum in 2014 and that Norway, Ireland, Liechtenstein, Switzerland, and Turkey are the largest e-waste generators with a total of 9.8 M tons and 20.4 kg/person/year in average, along with the United States (7.1 M tons and 22.3 kg/person) and China (6 M tons, 4.4 kg/person). There is a dramatic increase in per capita generation particularly in the developing countries (Gu *et al*., 2016; Yunus and Sengupta, 2016). A substantial increase in e-waste generation in developing countries is as a result of the forecasted economic growth (Yamane *et al*., 2011; Isildar *et al*., 2019).

Once these e-wastes are in the environment, they infiltrate into soil and even groundwater aquifer, causing environmental pollution. Thus, they can impair human health and environment. E-waste is therefore considered a major point source of potentially toxic elements/heavy metal pollutants in our modern cities. Strategies towards proper disposal, sorting, pretreatment and recovery of metals from e-waste are of current focus in advanced economies but are seriously lacking in our country leading to environmental pollution problems. This research will seek to convert discarded e-waste to useful products which might be relevant for uses in our industries and the world at large. Therefore, the aim of the study is to characterize raw and recovered e-waste metal oxides.

However, different characterization tools have been used to determine the mineral structure, morphology and elemental composition of representative e-waste samples. In order to obtain the particle size distribution, shape and morphology of representative sample of e-waste, before leaching treatments, Kolencik *et al*. (2013) used scanning electron microscopy (SEM) and energy dispersive X-ray microanalysis (EDX) to determine elemental composition. The results of the scanning electron micrographs showed noticeable differences in particle morphology and relative wide particle size distribution ranging from 0.01 µm to 150 µm.

Similarly, Alzate *et al*. (2016) recovered gold (Au) and the oxidized substrate and analyzed them using SEM/EDX in order to evaluate chemical composition and morphology. In their results, pure gold was removed as a fine coating from the substrate. The generated sulphates were chemically characterized by X-ray fluorescence spectroscopy (XRF) (Alzate *et al*., 2016). The particle size distribution of powdered printed circuit board (PCB) sample was characterized using a Mastersizer 2000 laser diffraction particle size analyser with a Scirocco 2000 Dry Powder Feeder (Ajiboye *et al*., 2019). The PCB sample was also characterized for elemental phases present using X-ray diffraction (X' Port Pro-PAN Analytical X-Ray Diffractometer (Model: EMPYREAN)). The morphological and phase identification was analyzed by SEM-EDX analysis (Ajiboye *et al*., 2019). Metallic copper foils obtained from waste PCBs using bioleaching and electrowinning processes were analyzed using a Carl Zeiss, 1530 VP field emission gun scanning electron microscope (FEG-SEM) and EDX analysis for morphology and purity respectively (Baniasadi *et al*., 2020).

In order to recover metals from mobile phone waste, Kim *et al*., (2018), examined the mineralogical characteristics of the precipitates formed via XRD, SEM with EDS analyses. XRD has also been used to determine the qualitative phase composition of a homogenous sample of tested battery mass (Urbanska, 2020). In recycling ceramic waste as a raw material in sanitary ware production, samples of powdered sanitary ware were characterized by X-ray fluorescence spectrometry (XRF), XRD and SEM (Silva *et al*., 2019).

2.0 Experimental

Samples of discarded e-waste pieces such as batteries, cell phones, laptops, radios and televisions were randomly collected from e-waste dumpsites and electronic workshops in Port Harcourt, Rivers State, Nigeria. The e-wastes collected were detached manually according to their kind as described by (Kolencik *et al*., (2013); Sahan *et al*., (2019). The individual components which include integrated circuit (IC), aluminium cover, condenser, capacitor, chopper transformer, transistor, battery, printed circuit board (PCB), diode and resistor were sorted out, de-soldered and subjected to incineration using the blacksmith flame as shown in plate 1. The pulverized samples obtained were crushed in a ceramic mortar and screened using a British Standard Sieve (BSS) 45 mm mesh for particle size distribution to obtain 1-2 mm size range particle size. These were packed in an air-tight polythene bags and taken to the laboratory for analyses. The ashed sample was characterised using XRD, SEM and EDXRF analyses.

Plate 1: Incinerated e-waste samples

Different characterization tools were used to identify and quantify the metals present in e-waste components including their morphology and mineral components. The X-ray diffraction (XRD) (Model: EMPYREAN) operating at an anode current of 40 mA at 45 kv with monochromatic Cu Kα1radiation source illustrated with Rietveld refinement method (Antao *et al*., 2008) was used to determine the mineral phases present in the raw and recovered e-waste The settings used included scan range of 4.9893-74.9997, scan angles of 2θ, 0-75° with step size of 0.0260 and scan step time of 23.9700 s. The XRD analysis was also used to determine the mineral structures present in the recovered products. This was equally done in order to know the inorganic materials present in the e-waste samples.

The particle size estimations were calculated from Scherrer's formula (Konne and Christopher, 2017) as illustrated in equation 3.1 below.

$$[d = \frac{k\lambda}{\beta \cos\theta}] \quad (1)$$

where;

$d$is mean particle diameter (size),

λ is Cu Kα1 radiation = 0.154 nm,

β is Full Width at Half Maximum (FWHM) (in radians), and

θ is half of 2θ angle (radians).

The morphological structure was performed using scanning electron microscopy (SEM) analysis, in order to obtain the various micrographs. The Fourier-Transform Infrared Spectroscopy (F-TIR) analysis was used to identify the functional groups present in the pure extracts obtained from the e-wastes. The energy dispersive x-ray fluorescence (EDXRF) Analysis was used to determine

the elemental composition of representative sample of e-waste, in order to identify the various elements in the minerals.

3.0 Results and Discussion

3.1 Characterization of E-wastes Using XRD

Table 1: Average Values of Particle Size Estimations from XRD Analysis Results for Samples A – J

S/N	Sample	E-waste Component	Mean Sizes (nm) (Raw)	Mean Sizes (nm) (Recovered)
1	A	Integrated Circuit	**72.19**	**58.48**
2	B	Aluminium Cover	46.04	Less crystalline
3	C	Condenser	45.76	14.61
4	D	Capacitor	33.38	31.58
5	E	Chopper Transformer	45.20	45.94
6	F	Transistor	47.05	14.33
7	G	Battery	**22.06**	**7.22**
8	H	Printed Circuit Board (PCB)	32.72	33.46
9	I	Diode	56.47	47.65
10	J	Resistor	53.93	15.77

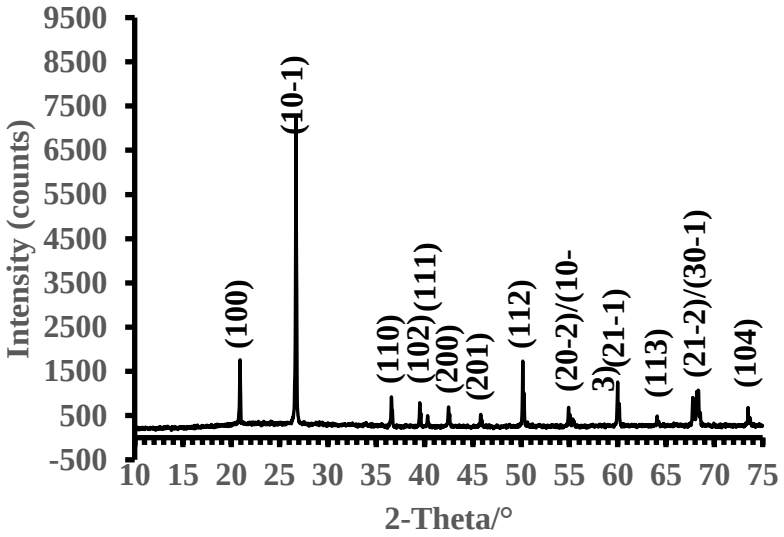

1 (a) XRD Patterns for Raw Sample A (Integrated Circuit)

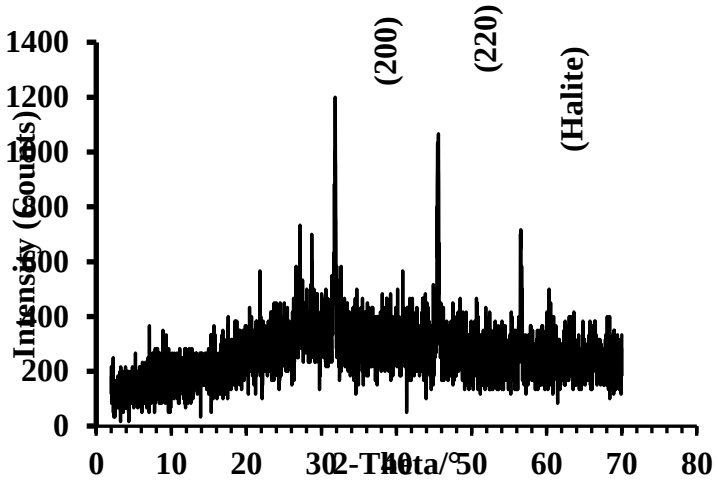

1 (b) XRD Patterns for Recovered Sample A (Integrated Circuit)

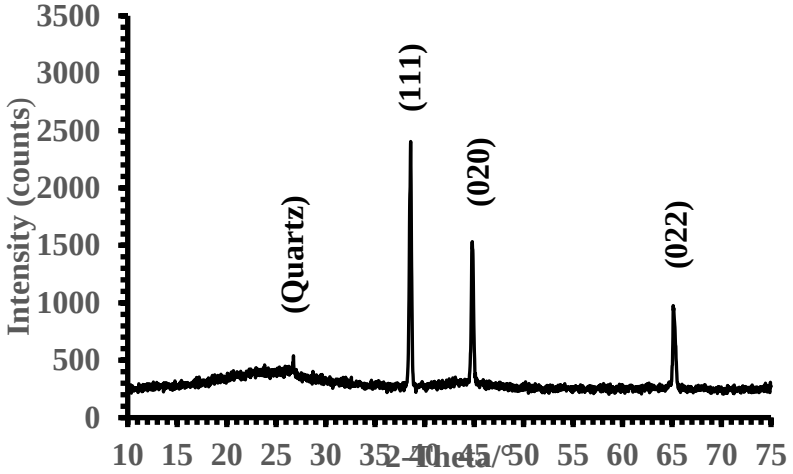

1 (c) XRD Patterns for Raw Sample B (Aluminium Cover)

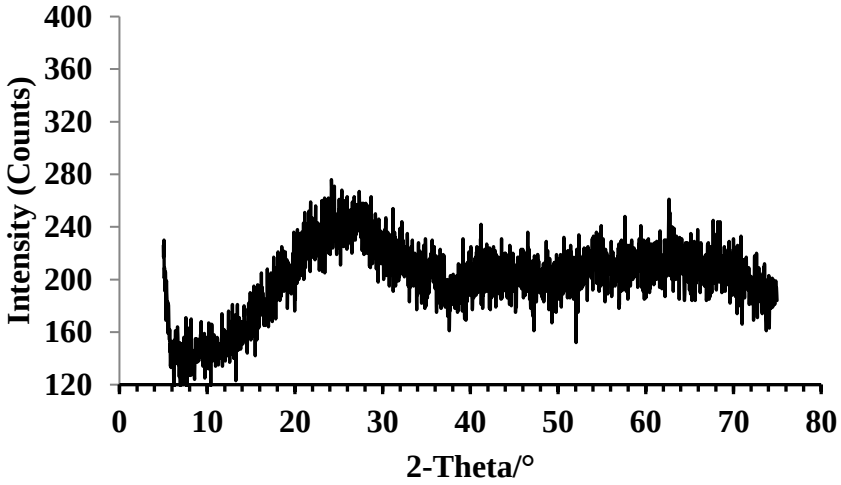

1 (d) XRD Patterns for Recovered Sample B (Aluminium Cover)

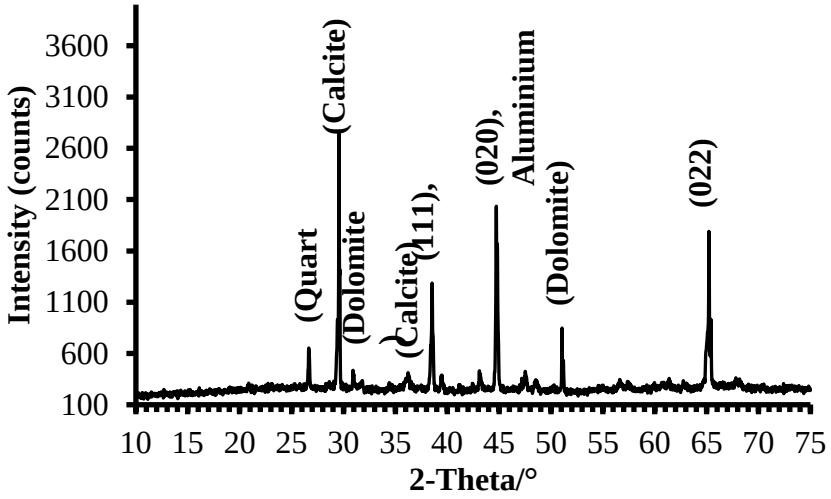

1 (e) XRD Patterns for Raw Sample C (Condenser)

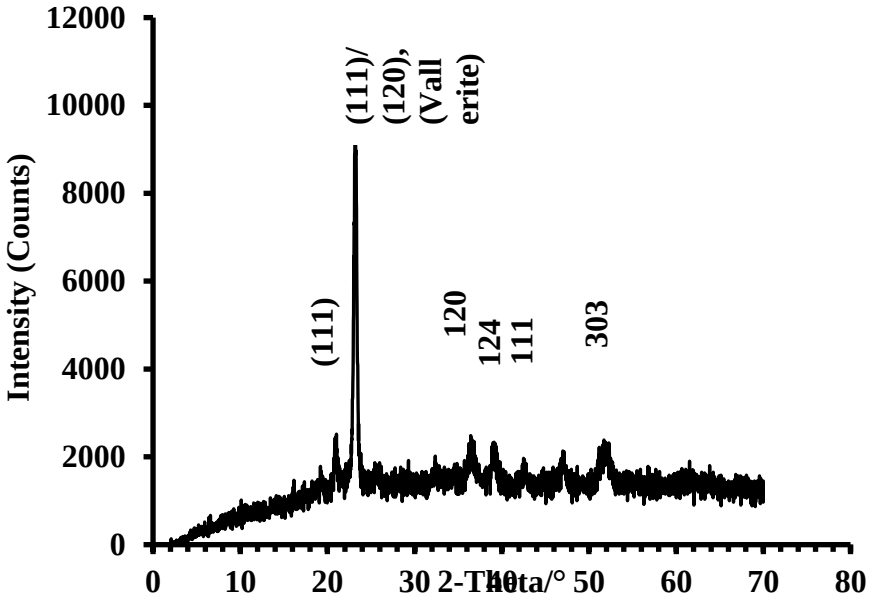

1 (f) XRD Patterns for Recovered Sample C (Condenser)

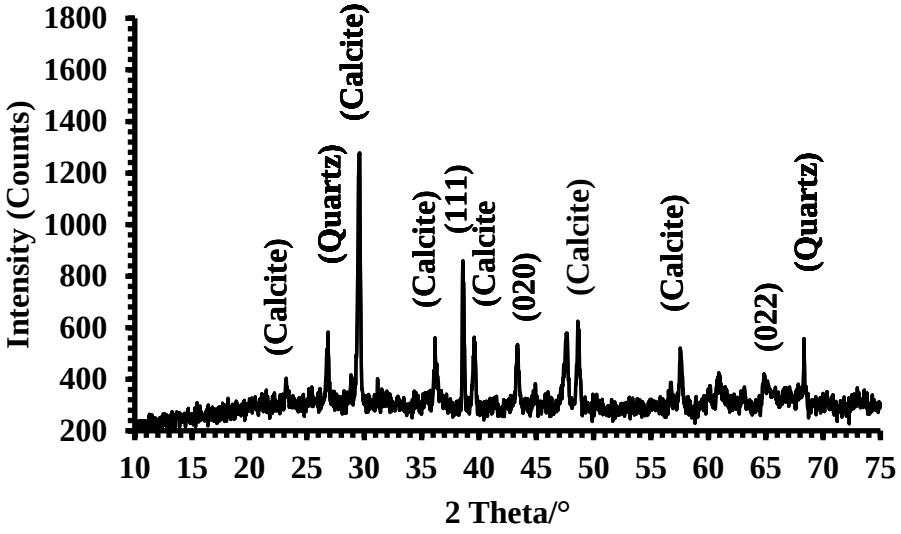

1 (g) XRD Patterns for Raw Sample D (Capacitor)

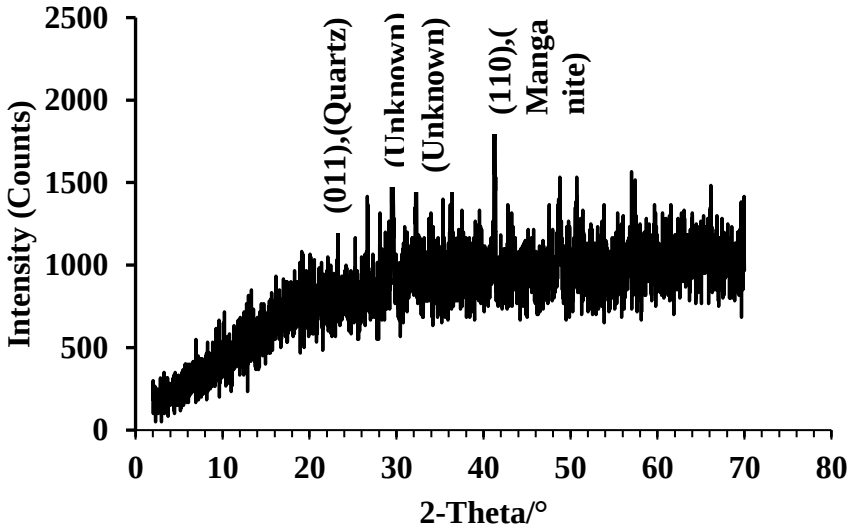

1 (h) XRD Patterns for Recovered Sample D (Capacitor)

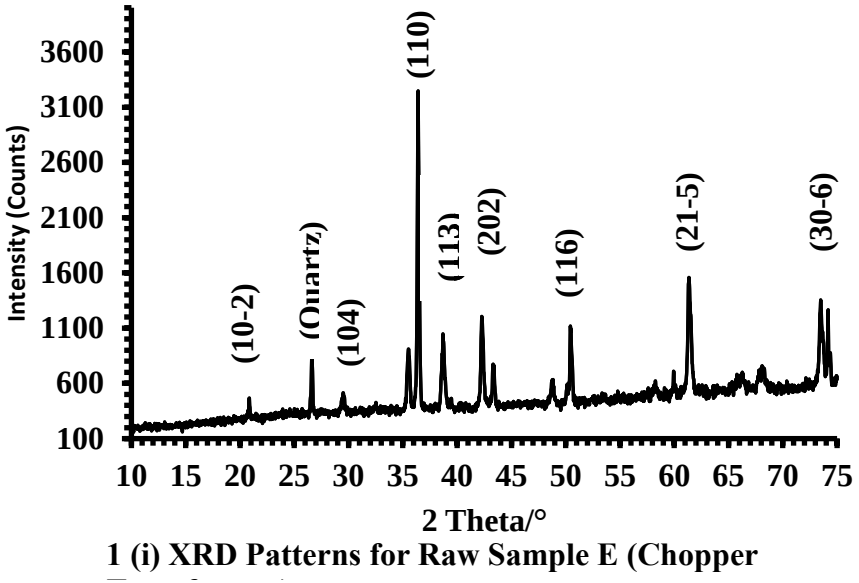

1 (i) XRD Patterns for Raw Sample E (Chopper

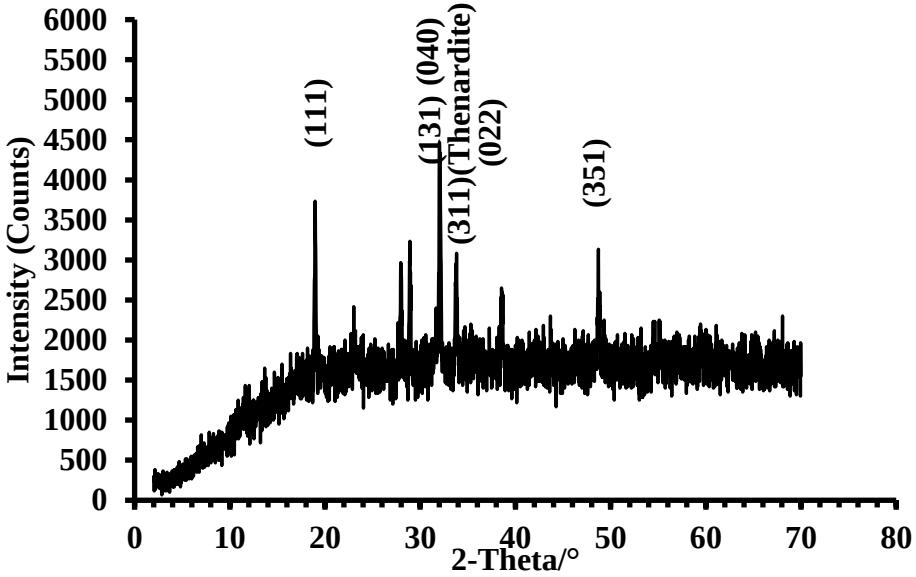

1 (j) XRD Patterns for Recovered Sample E (Chopper Transformer)

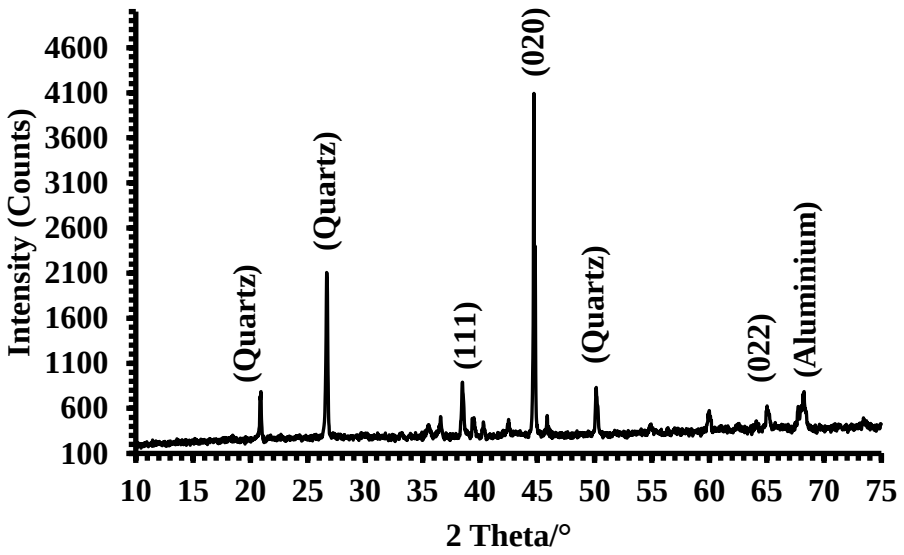

1 (k) XRD Patterns for Raw Sample F (Transistor)

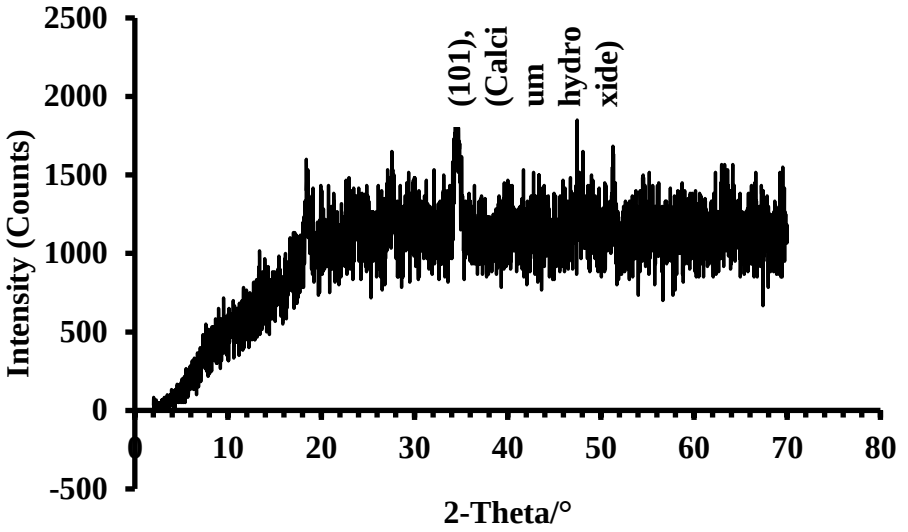

1 (l) XRD Patterns for Recovered Sample F (Transistor)

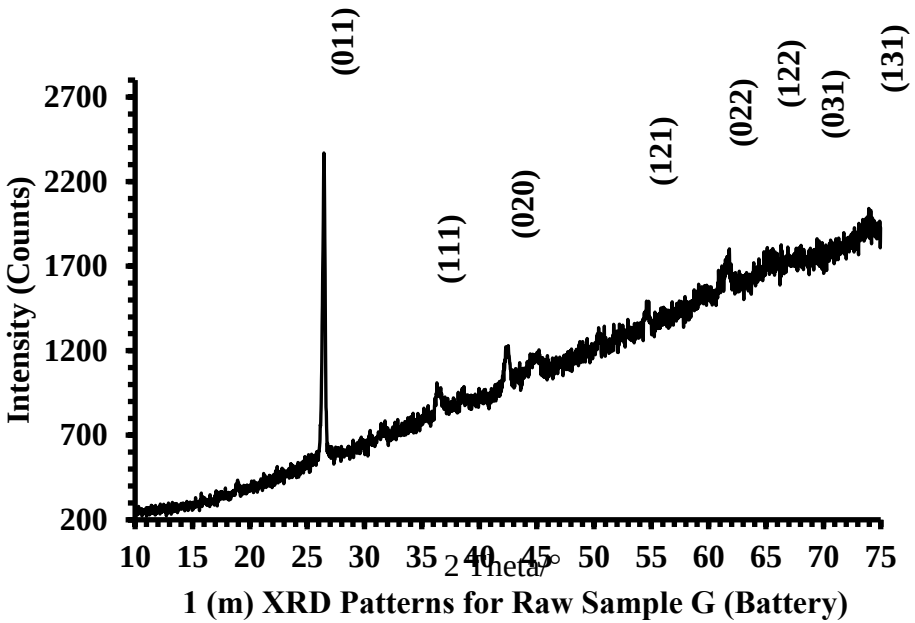

1 (m) XRD Patterns for Raw Sample G (Battery)

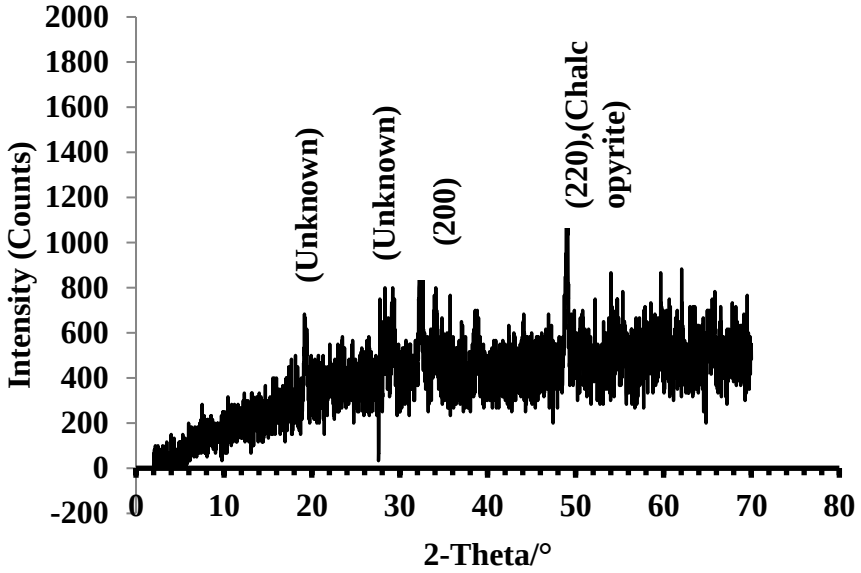

1 (n) XRD Patterns for Recovered Sample G (Battery)

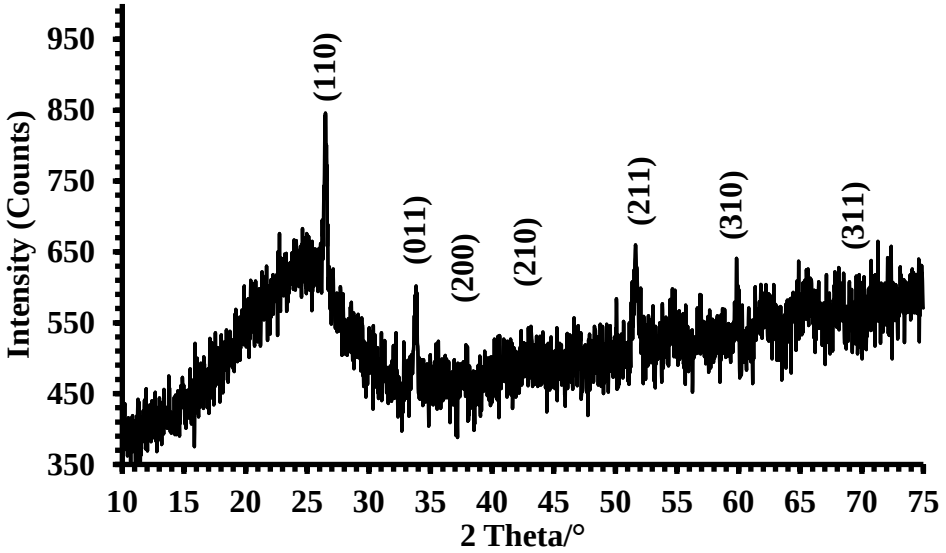

1 (o): XRD Patterns for Raw Sample H (PCB)

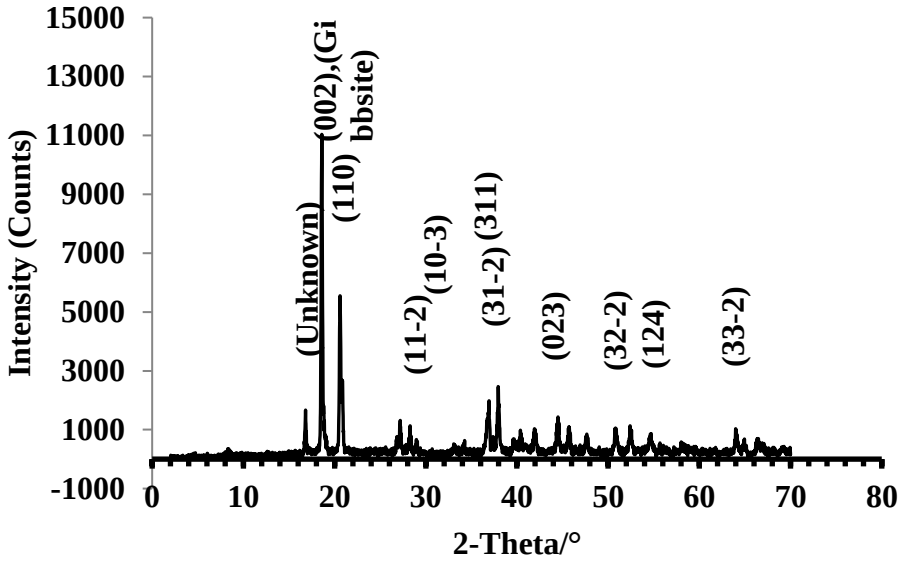

1 (p) XRD Patterns for Recovered Sample H (PCB)

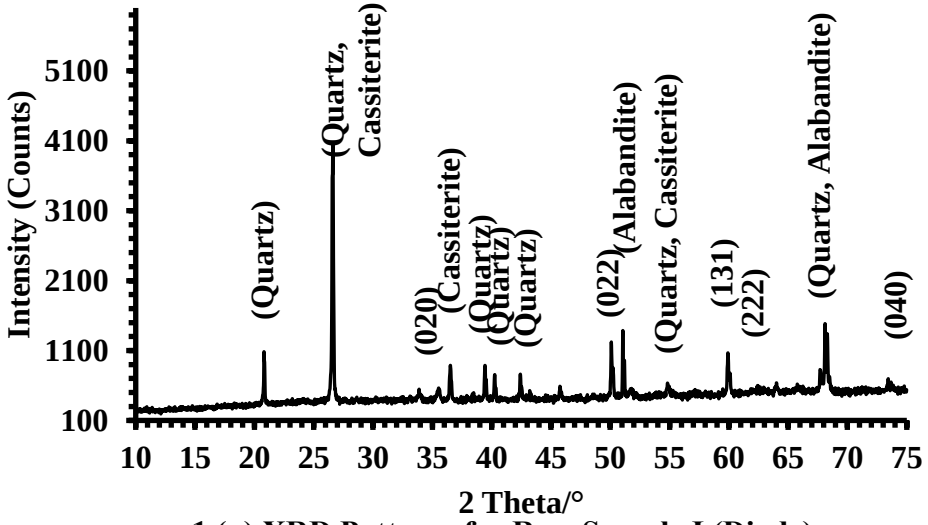

1 (q) XRD Patterns for Raw Sample I (Diode)

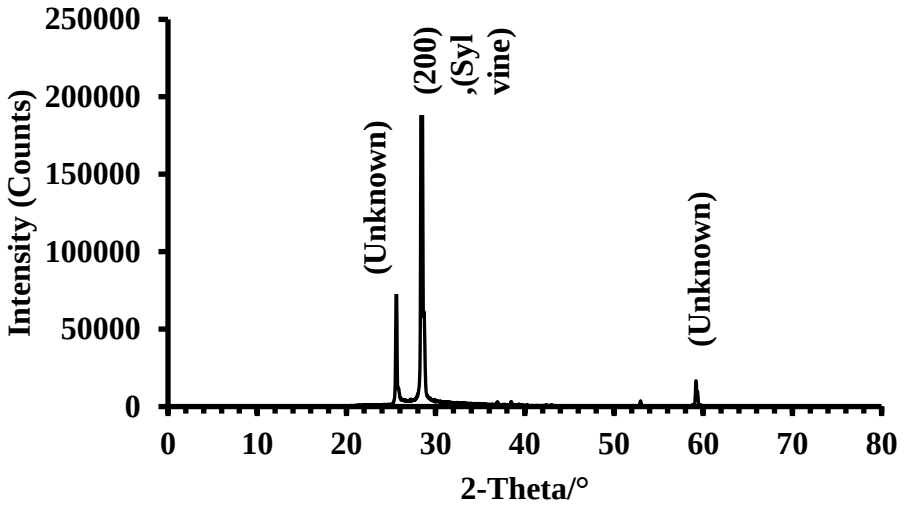

1 (r): XRD Patterns for Recovered Sample I (Diode)

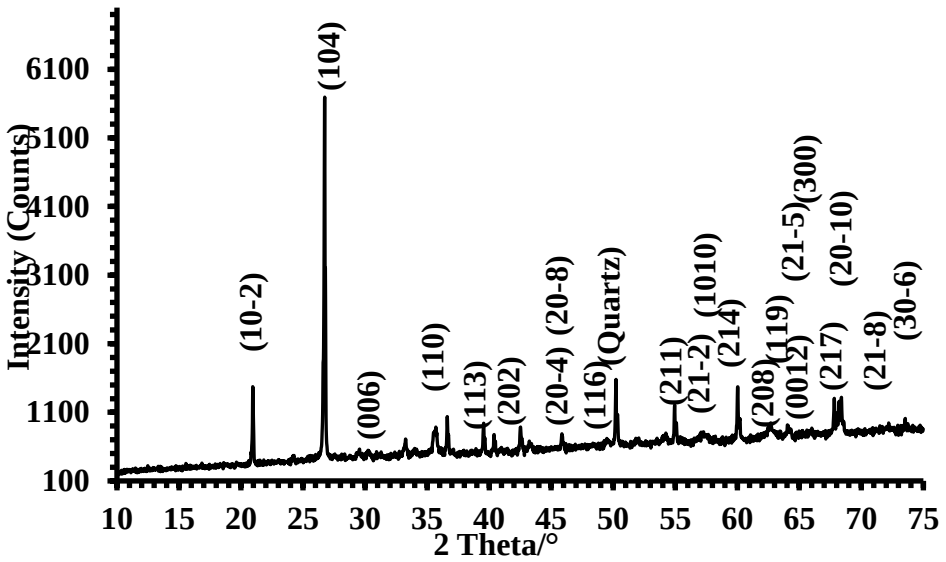

1 (s) XRD Patterns for Raw Sample J (Resistor)

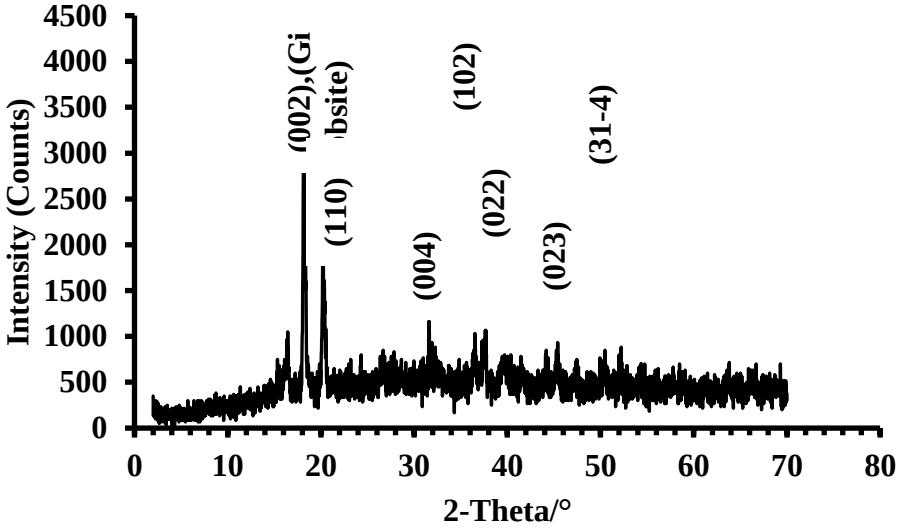

1 (t) XRD Patterns for Recovered Sample J (Resistor)

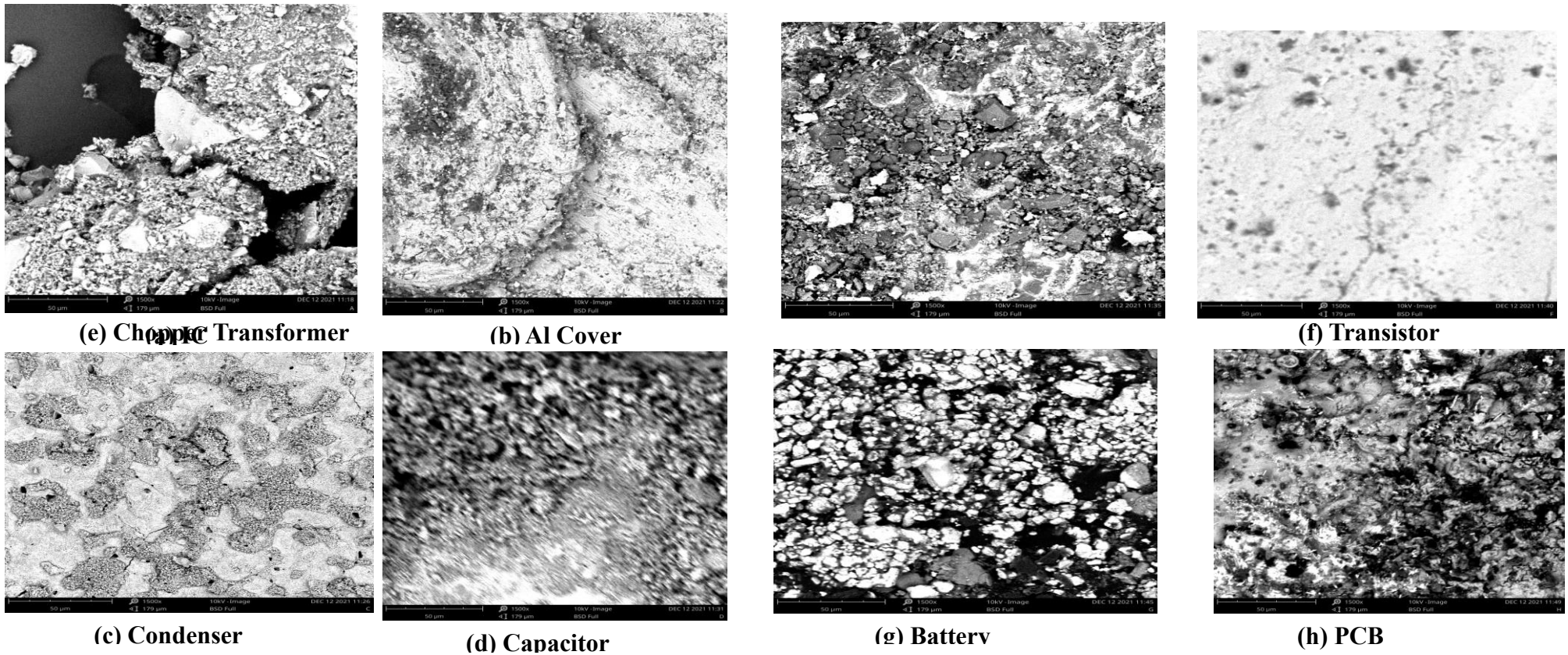

Figure 2: Scanning Electron Micrographs Showing Surface Morphology of Samples a to j

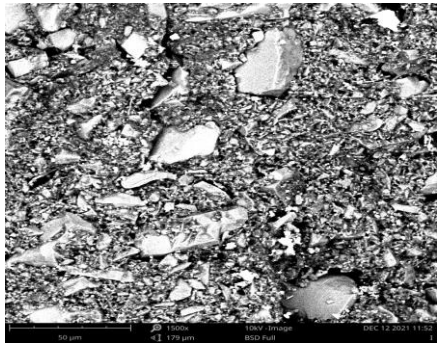

(i) Diode

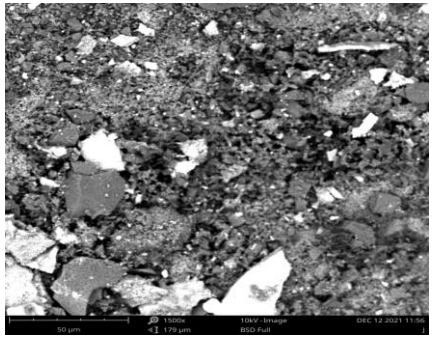

(i) Resistor

3 (e) FTIR Spectrum of Recovered Sample E (Chopper transformer)

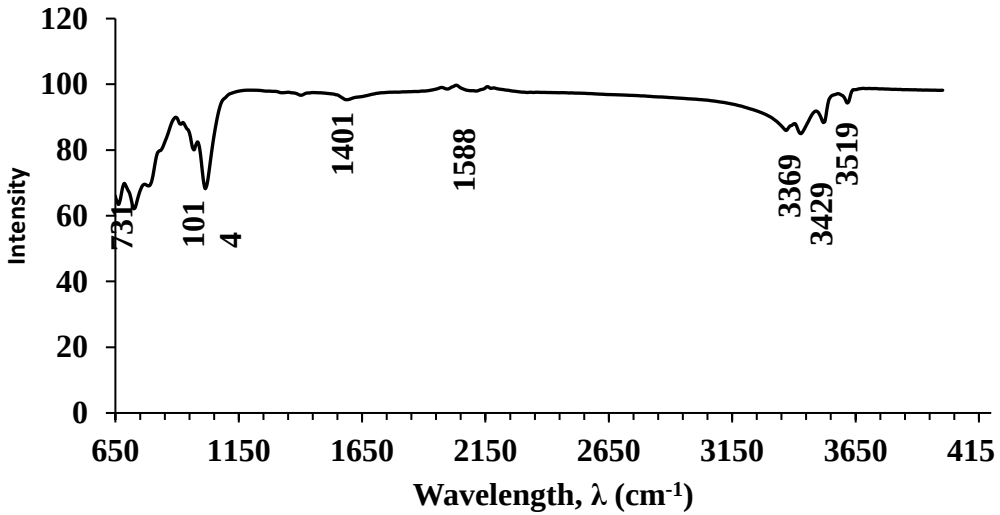

3 (f) FTIR Spectrum of Recovered Sample F (Transistor)

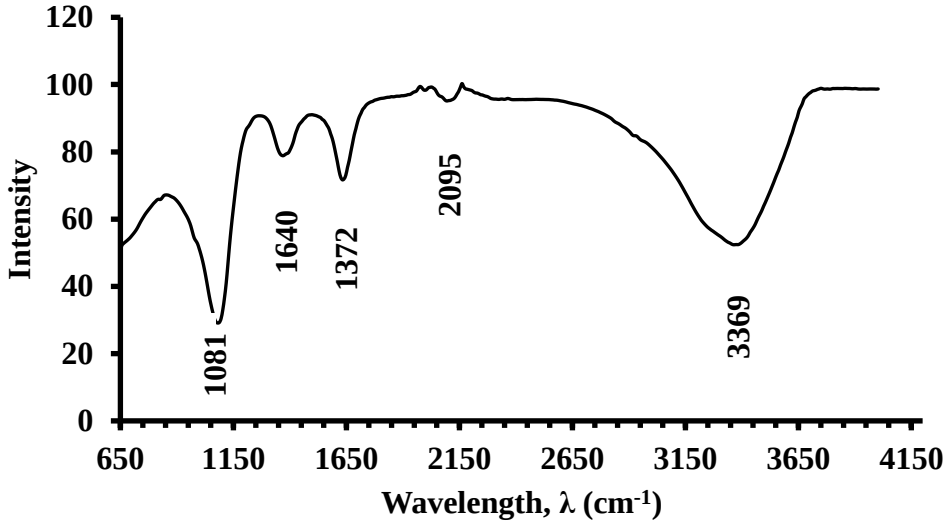

3 (b) FTIR Spectrum of Recovered Sample B (Aluminium cover)

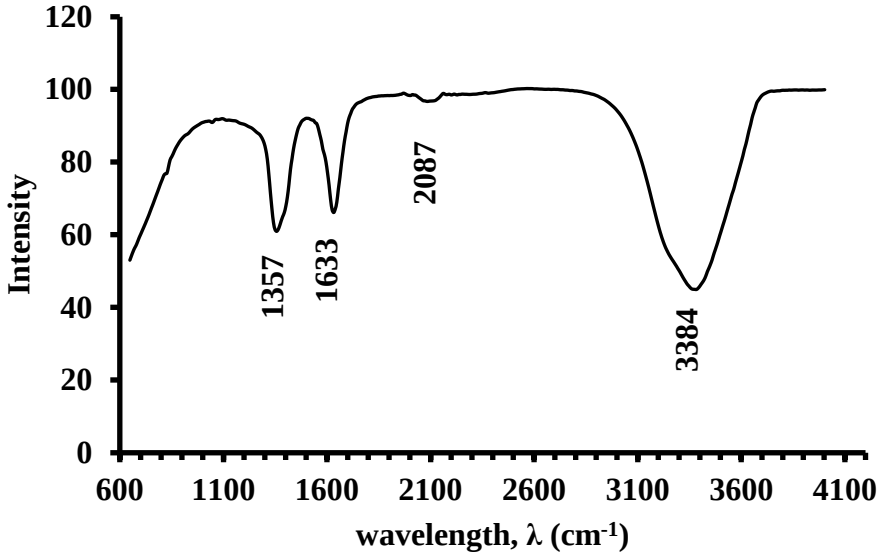

3 (a) FTIR Spectrum of Recovered Sample A (I.C)

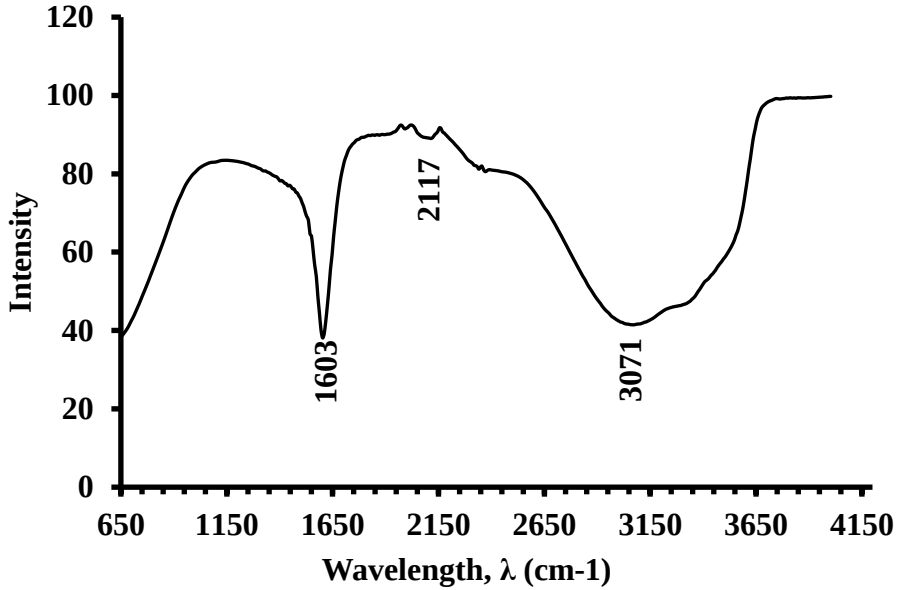

3 (d) FTIR Spectrum of Recovered Sample D (Capacitor)

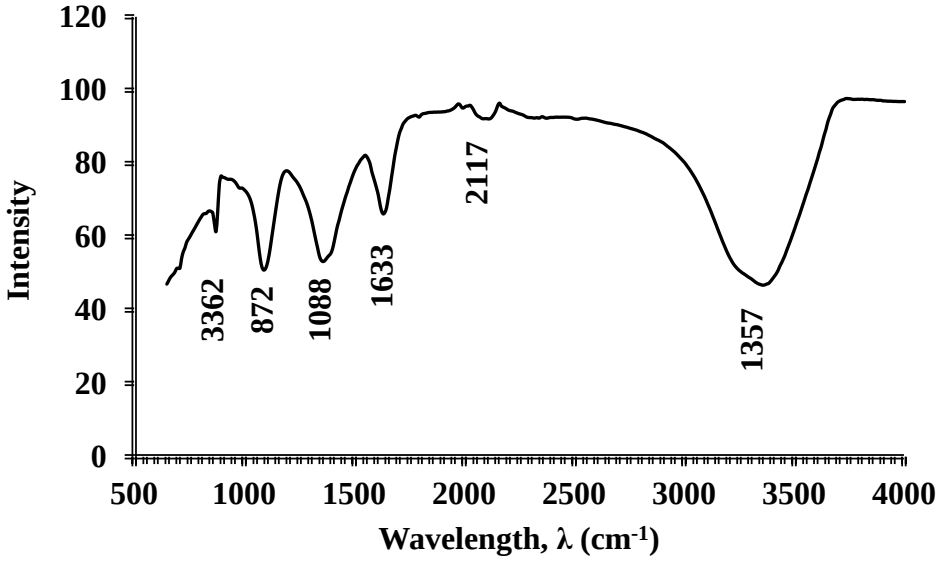
Intensity
120
100
80
60
40
20
0
500
1000
1500
2000
2500
3000
3500
4000
Wavelength, λ (cm-1)
3362
872
1088
1633
2117
1357

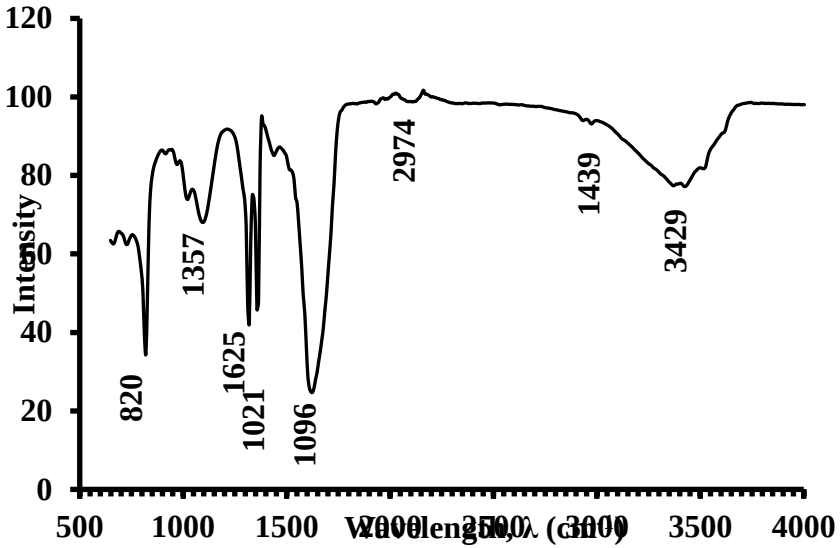
Intensity
120
100
80
60
40
20
0
500
1000
1500
3500
4000
820
1357
1625
1021
1096
2974
1439
3429

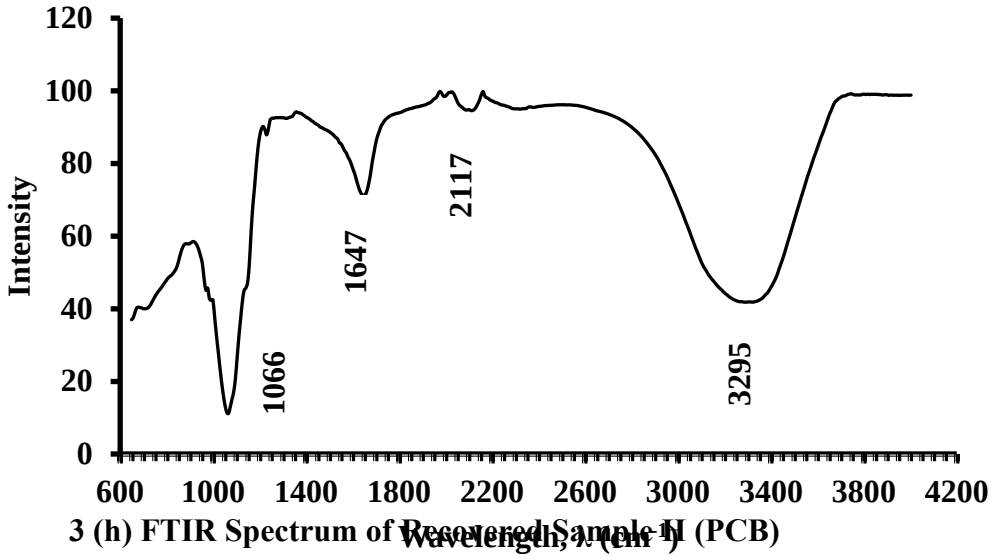

3 (h) FTIR Spectrum of Recovered Sample H (PCB)

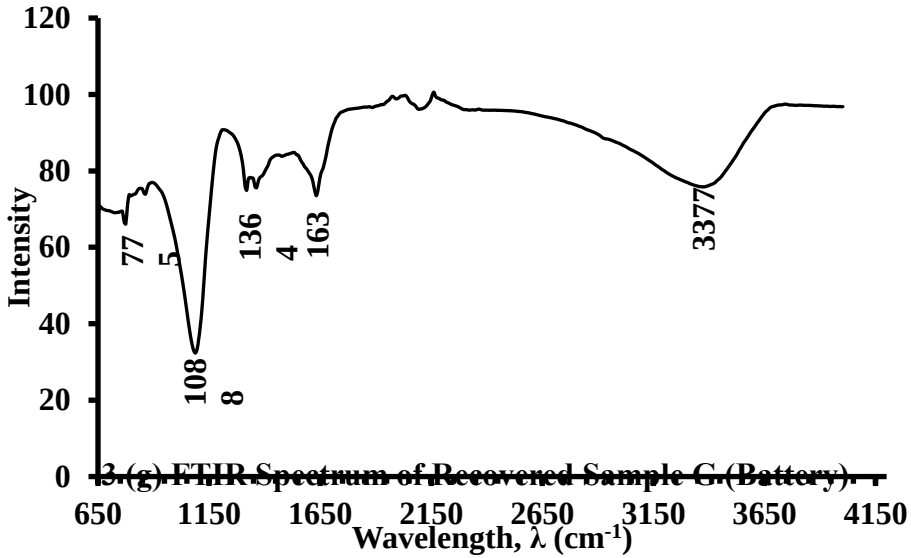

3.(g) FTIR Spectrum of Recovered Sample G.(Battery).

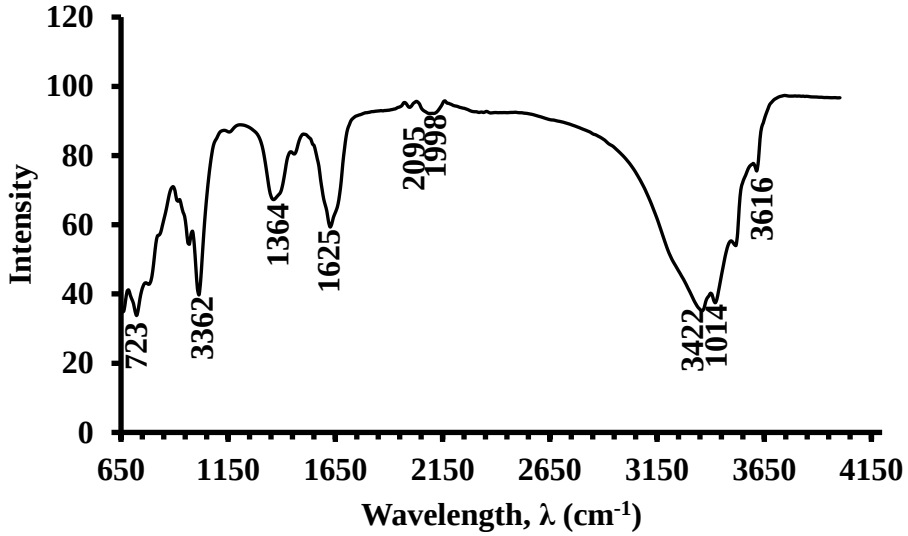

3 (j) FTIR Spectrum of Recovered Sample J (Resistor)

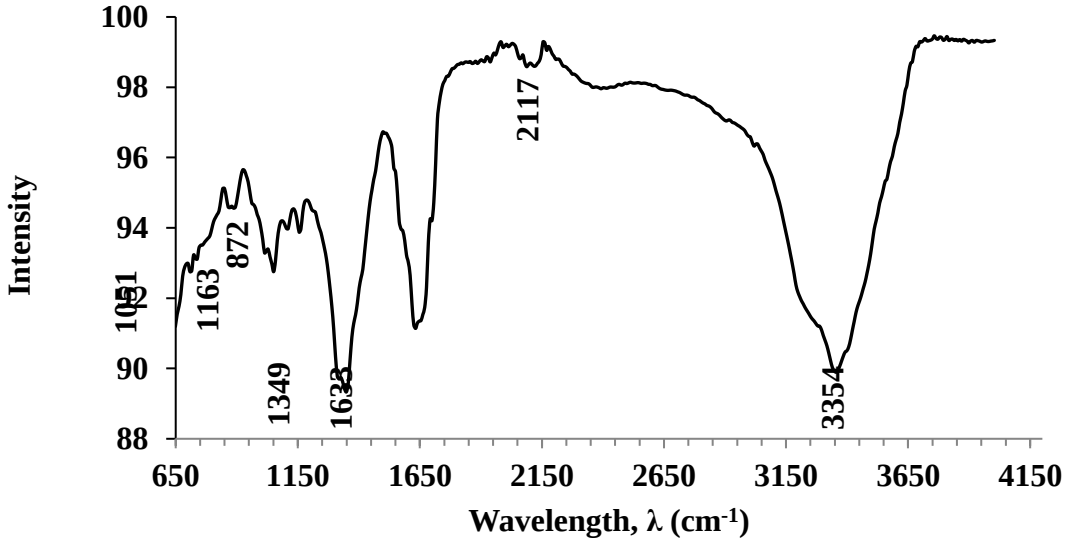

3 (i) FTIR Spectrum of Recovered Sample I (Diode)

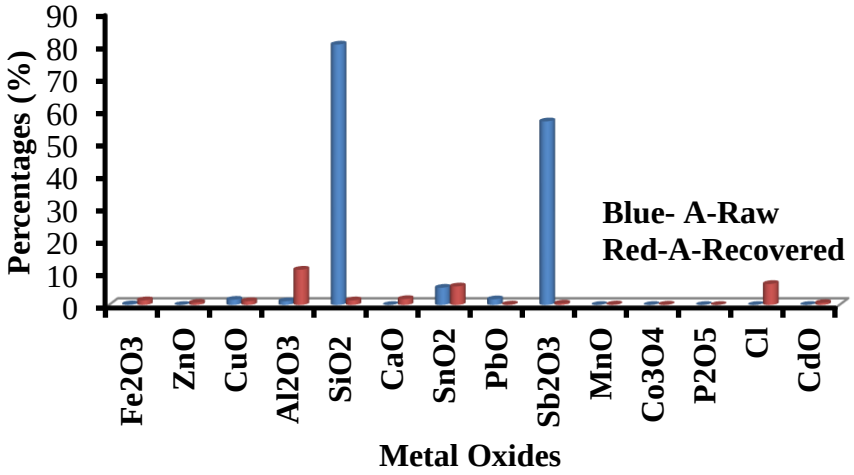

4 (a): Composition of Metal Oxides in Raw and Recovered E-waste Sample A

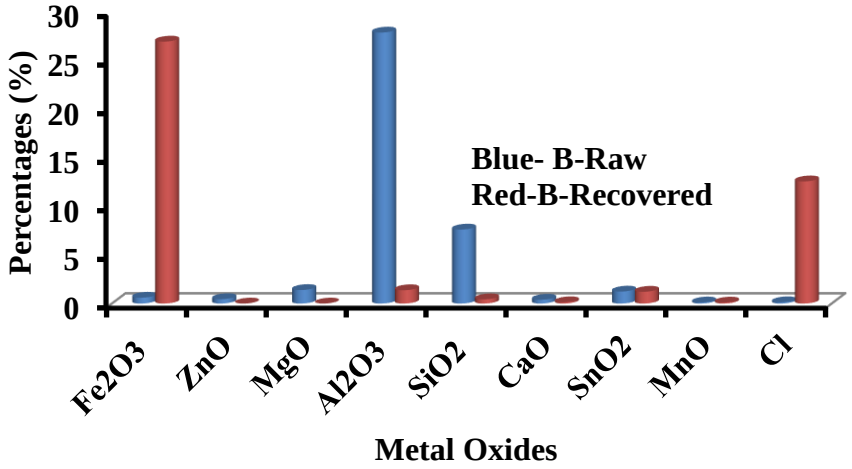

4 (b): Composition of Metal Oxides in Raw and Recovered E-waste Sample B

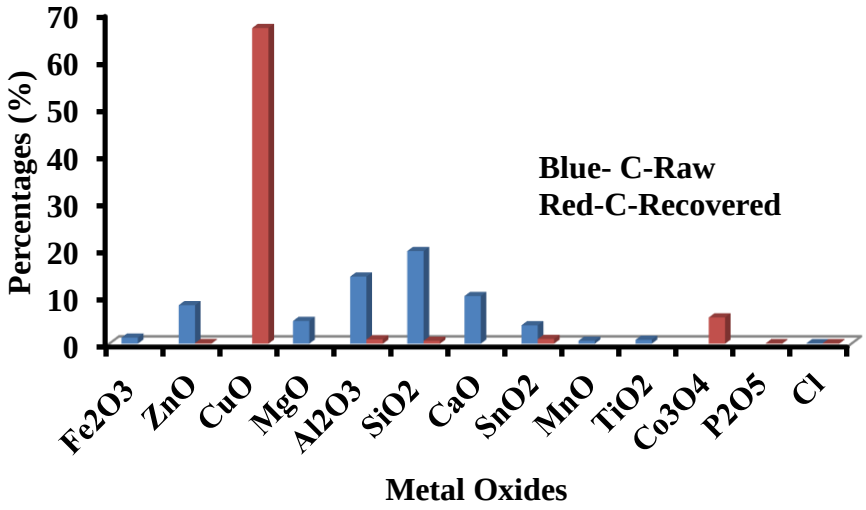

4 (c): Composition of Metal Oxides in Raw and Recovered E-waste Sample C

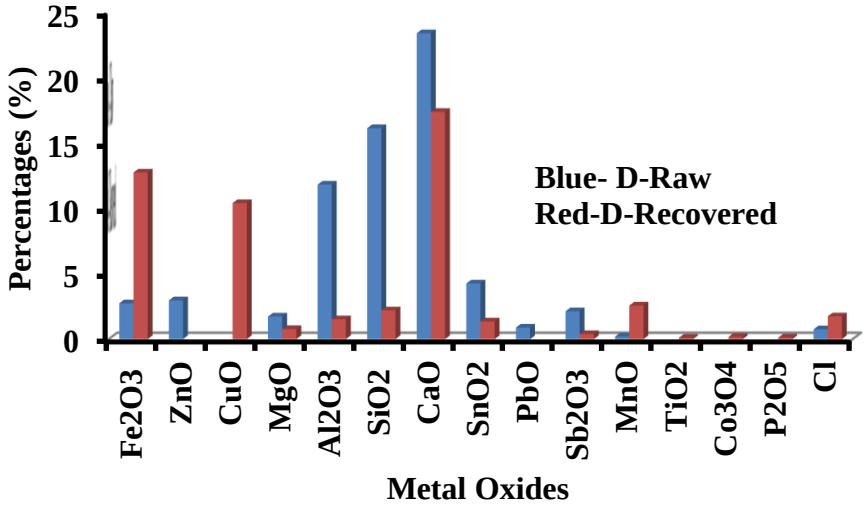

4 (d): Composition of Metal Oxides in Raw and Recovered E-waste Sample D

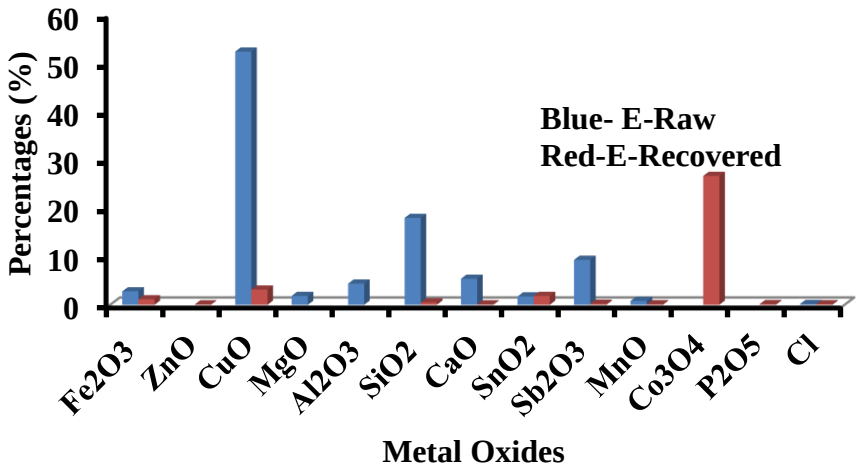

4 (e): Composition of Metal Oxides in Raw and Recovered E-waste Sample E

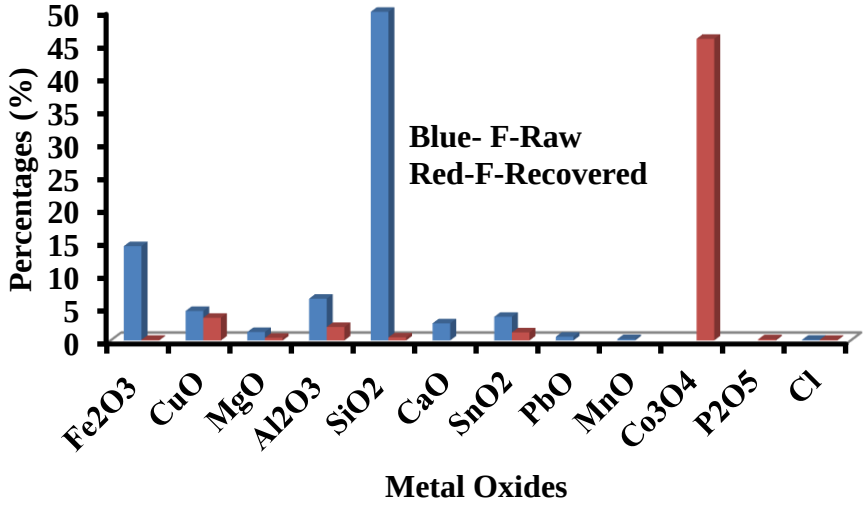

4 (f): Composition of Metal Oxides in Raw and Recovered E-waste Sample F

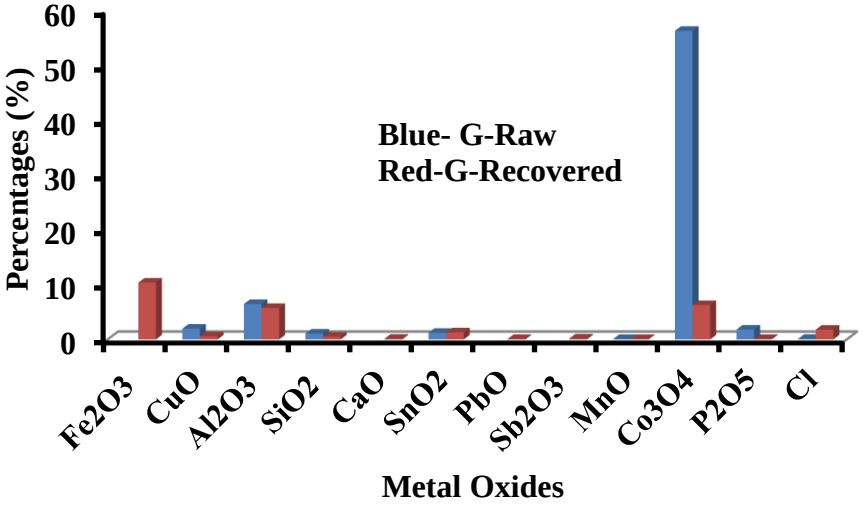

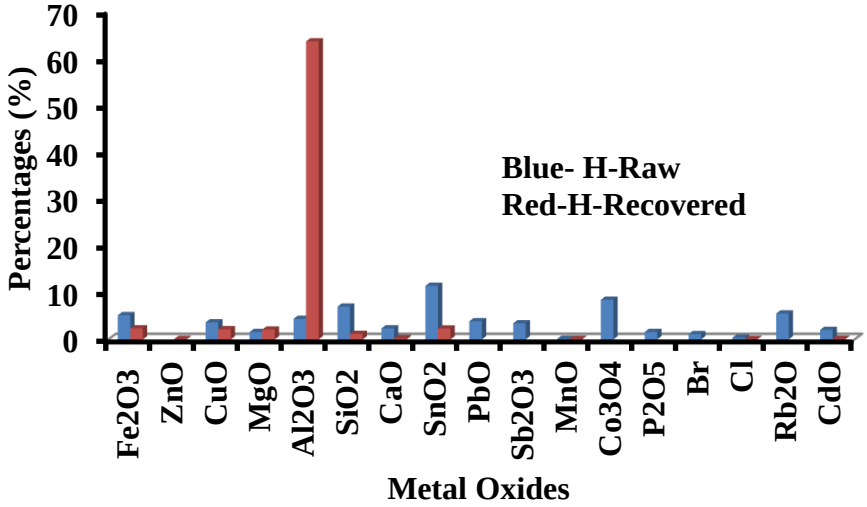

4 (g): Composition of Metal Oxides in Raw and Recovered E-waste Sample G

4 (h): Composition of Metal Oxides in Raw and Recovered E-waste Sample H

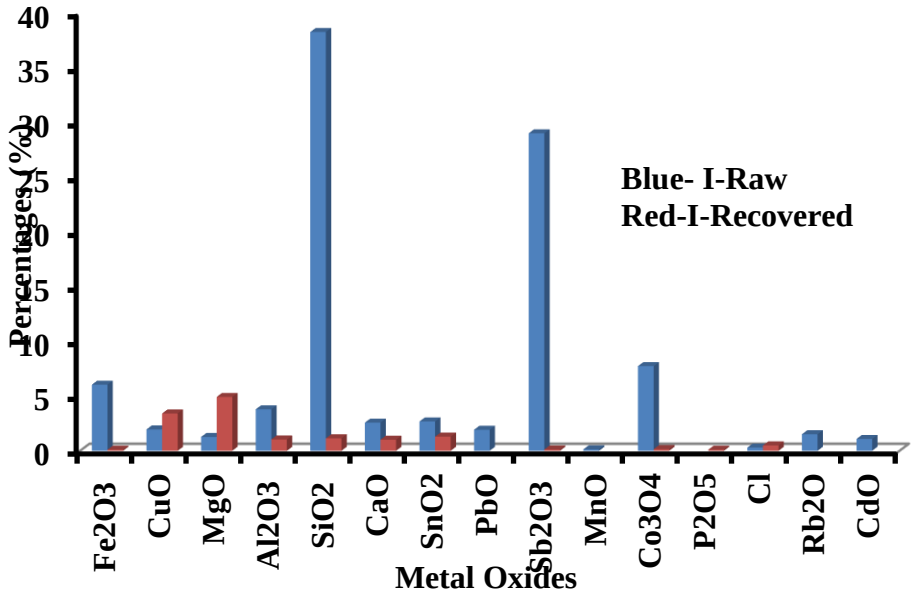

4 (i): Composition of Metal Oxides in Raw and Recovered E-waste Sample I

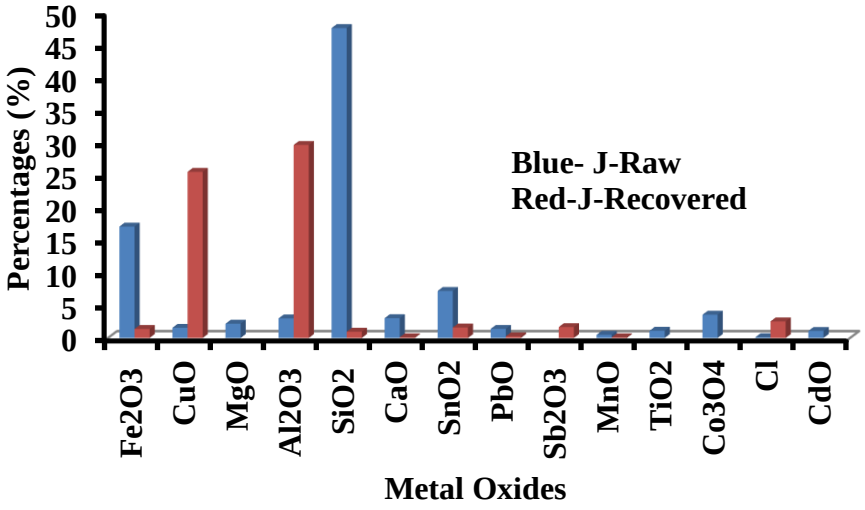

4 (j): Composition of Metal Oxides in Raw and Recovered E-waste Sample J

3.1 Characterization of E-wastes Using XRD

The results of the average values of particle size estimations from XRD analysis for raw samples A to J as presented in Table 4.1 showed that sample A (Integrated circuit) had the highest mean size (72.19 nm) while sample G (battery) had the least mean size (22.06 nm). Also, for recovered products, sample A had the highest mean size (58.48 nm) and sample G, the least (7.22 nm), although sample K had a negative value (-12.79 nm). This shows that sample A had the largest particle size while sample G, the smallest particle size. However, recovered sample B had no mean size as it was less crystalline or amorphous. These generally indicate heterogeneous particle size distribution across the samples. The values at 2-Theta (degree) and full width at half maximum (FWHM) were calculated to obtain the sizes, with the average values. In fact, the mean sizes are in the order: A > I > J >F >B >C >E >D >H > G and A > I > E > H > D > J > C > F > G respectively.

3.2 XRD Patterns for E-waste Samples

The XRD patterns of e-waste as shown in Figures 1 (a) to (t) are plots of intensities (counts) against 2-Theta. In the XRD patterns of raw sample A (Integrated circuit) (Figure 1a), the highest peak with hkl (10-1) showed (Quartz, Si_3O_6); 100 %, as the only mineral phase at a 2-Theta value of 26.70 °. The major reflections of raw sample A were indexed to hexagonal synthetic quartz of the space group, P 31 2 1, using the Crystallography Open Database (COD) files number 9013321 (Antao *et al*., 2008) and this matched with the quartz phases as reported by Silva *et al*. (2019). The major reflections of raw sample A also matched with the reflections reported by Zhang *et al*. (2020) and Deng *et al*. (2019).

In the XRD patterns of recovered sample A (Integrated circuit) (Figure 1 b), the highest peak with hkl (220) showed (Halite, NaCl); 82.1 %, as the major mineral phase at a 2-Theta value of 45.45 ° with traces of Urea (CH_4N_2O; 17.9%). Figure 1 b showed bumpy reflections, possibly due to background noise. This could be attributed to impurities present in the sample that are less crystalline. The major reflections matched with the reflections obtained by Lopez-Juarez *et al*., (2018) for the XRD patterns of aluminum acetate and powders heat treated at different temperatures for 3 h and Feng-Hua *et al*. (2014) for the XRD pattern of $Ni_{42.8}Mn_{40.3}Co_{5.7}Sn_{11.2}$ alloy at room temperature.

In raw sample B (Aluminium cover), the XRD patterns with hkl (111) showed the major mineral phase (Aluminium, Al_4; 96%) at a 2-Theta value of 38.60 °, with a minor quantity of quartz (Figure 1 (c). The XRD patterns of raw sample B matched with the XRD patterns reported by Guan *et al*. (2018), John *et al*. (2018) and Kaur and Pandey (2013).
The diffraction patterns of the XRD analysis for recovered sample B (Aluminium cover) as shown in Figure 1 (d) displayed a very broad humped peaks instead of crystalline peaks and scattered at different angles, confirming a short range order characteristics of amorphous sample (Madheshiya *et al*., 2017). Therefore, there is no mineral phase name and chemical formula attached to it.

The XRD Patterns of e-waste raw sample C (Condenser) showed the highest peak with hkl (020) with a 2-Theta value of 44.71 ° as aluminium; 41.8 % (major mineral structure). However, the

counts (peak) at a 2-Theta value of 29.58 °, showed calcite ($Ca_6C_6O_{18}$), followed by quartz (Si_3O_6) and dolomite ($Ca_3Mg_3O_6$ O_{18}) as minor mineral structures (Figure 1 (e). These patterns or reflections matched exactly with those observed by Zhao *et al*. (2020).
The XRD patterns of recovered sample C (Condenser) (Figure 1 f), had the highest peak with hkl (111) showing Vallerite ($Cu_2Fe_4S_7$; 70.2 %) as the prominent mineral structure at a 2-Theta value of 29.97 ° alongside 28.2 % Moolooite ($C_2CuO_4.xH_2O$ and 1.66 % Crystobalite (SiO_2). The XRD patterns of recovered sample C matched with the patterns reported by Agbaei *et al*. (2020).

The XRD patterns of e-waste for raw sample D (Capacitor) (Figure 1 g) identified calcite ($Ca_6C_6O_{18}$; 74.3 %) as the major mineral structure and it is very prominent at a 2-Theta value of 29.59 °, with traces of aluminum and quartz. The highest peak with hkl (111) has a 2-Theta value of 38.59 °. The XRD patterns of raw sample C matched with the XRD patterns of calcium silicate bioceramic materials prepared by Sol-Gel (SG) synthesis calcined at (A): 600 °C and (B): 950 °C (Arslan *et al*., 2019). The recovered sample D (Figure 1 h) showed the highest peak with hkl (110) and Manganite ($Mn_2O_3H_7O$; 76.8 %) as the prominent mineral phase. Little quantities of quartz and manganese-delta (Mn) are equally observed in the sample. All the peaks are very blunt; indicating that there are crystallinity impurities. Hence, the sample had low purity. The major reflections of the XRD patterns matched with the XRD patterns for conventionally solidified Al-Cu-Fe alloys (Gogebakan *et al*., 2009).
For raw sample E (Chopper Transformer), the mineralogy comprises quartz (60 %), tenorite, (Cu_4O_4), 32 % and calcite, ($CaCO_3$), 8 % as displayed in Figure 1 (i). The major mineral structure (Quartz) is noticed at a 2-Theta value of 36.39 °, with hkl (110). The XRD patterns tallied with XRD patterns of CuO nanomaterials (Ashok *et al*., 2014) and XRD pattern of synthesized CuO nanoparticles (Padil and Cernik, 2013). The quantitative mineralogical analysis by the XRD Patterns of recovered sample E (Figure 1 j) showed a well-defined presence of Thenardite, Na_2SO_4, phases (97.80 %) with very low silver chloride (AgCl) phases (2.20 %). The major reflections matched with Agbaei *et al*. (2020).
The XRD Patterns of e-waste raw sample F (Transistor) identified quartz as the major mineral phase (71%) at a 2-Theta value of 45.83 ° with hkl of (020) and traces of aluminium and hematite ($Fe_{12}O_{18}$) (Figure 1 (k). Hiraga *et al*. (2021) also identified hematite with very low aluminium in the Brazilian iron ores. The XRD patterns of raw sample F matched with the XRD patterns reported by Xu *et al*. (2019) and Gao and Liu, (2017).

The XRD Pattern of e-waste recovered sample F (Transistor) (Figure 1 l), showed the highest peak with hkl (101) at a 2-Theta value of 34.49 ° bearing calcium hydroxide, $Ca(OH)_2$, 89.4 %, as the main mineral phase and sylvite, KCl (10.6 %) as a minor mineral phase. The humped peaks with a short range ordering indicate the near amorphous nature of recovered sample F. However, the XRD patterns matched with those of Huo *et al*. (2017). The hkl of raw sample G (Battery) (011) showed the major mineral phase as quartz (82 %) at a 2-Theta value of 26.47 ° and traces of cuprite (Cu_4O_2) (Figure 1(m). The XRD patterns for raw sample G agrees with the X-ray diffraction pattern of crystalline boron oxide (Tran *et al*,. (2018). The recovered sample G identified Chalcopyrite, $CuFeS_2$ (85 %) as the major mineral phase via XRD analysis. The recovered sample G also contains 15 % halite. Chalcopyrite has hkl (220) (Figure 1(n). The XRD pattern of recovered

sample G matched with those reported by Qi *et al*., (2013) and corresponds with the XRD patterns showing the presence of Chalcopyrite as documented by Nyamjargal *et al*., (2018) and Zavasnik *et al*. (2014).

The XRD Pattern of e-waste raw sample H (PCB) as displayed in Figure 1(o) which is a plot of intensity (counts) against 2-Theta shows cassiterite (Sn_2O_4) as the major or only mineral structure. The highest peak has hkl (110) at a 2-Theta value of 26.50 °. Ajiboye *et al*. (2019) had also documented the presence of cassiterite in their XRD pattern of powdered PCBs sample. The XRD patterns for raw sample H matched with the XRD pattern of the tin oxide powder reported by Nilchi *et al*. (2013). For recovered sample H, Figure 1(p), Gibbsite, Al $(OH)_3$ with hkl (002), is the major mineral (84.1%) with traces of Orthoclase ($Al_2O_3.K_2O_6.SiO_2$). It matched with the XRD patterns reported by Karipoth *et al*. (2016).

The XRD Pattern of e-waste raw sample I (Diode) as displayed in Figure 1 (q) showed the highest peak with hkl (022) at a 2-Theta value of 51.06 °, and this matched with the XRD patterns recorded by Pang *et al*. (2014). It is also similar with the XRD patterns of raw sample A which matched with the XRD patterns of Deng *et al*., (2019). It identifies quartz as the major mineral structure (85 %) with traces of alabandite (Mn_4S_4) and cassiterite (Sn_2O_4). The recovered sample I identified Sylvine, Sodian (KO.7NaO.3Cl) (71 %) as the major mineral phase and Sylvite (KCl); 29 % via XRD analysis. Sylvine, Sodian, has the highest peak with hkl (200) at a 2-Theta value of 28.49 ° (Figure 1 r). This matched with the XRD patterns reported by Beaulieu *et al*. (2003).
The XRD Pattern of e-waste raw sample J (Resistor) (Figure 1 s) indicated the highest peak with hkl (104) at a 2-Theta value of 29.50 ° and shows quartz (72.7 %) as the major mineral structure with traces of hematite ($Fe_{12}O_{18}$), magnetite ($Fe_{24}O_{32}$) and calcite. Its XRD patterns matched with the XRD spectra of control and bioremediated sample in Raja *et al*., (2022). In an XRD pattern reported by Mishra and Lee (2018), magnetite was confirmed in a metallic iron (Fe) phase. In another quantitative mineralogical analysis using XRD, hematite, magnetite and quartz were identified in iron ores (Hiraga *et al*. (2021). In fact, hematite and magnetite were the major minerals in the Carajas iron ore. The XRD pattern of powdered PCBs sample had also shown the presence of hematite and magnetite as major metal oxides (Ajiboye *et al*., 2019). The recovered sample J (Figure 1 t) identified Gibbsite, Al $(OH)_3$, (96.6 %) as the major mineral phase with just 3.4 % quartz (minor mineral) via XRD analysis. Gibbsite has the highest peak with hkl (002) at a 2-Theta value of 18.19 ° (Figure 1 t). Its XRD patterns matched with the XRD spectra of crystalline phase of Al $(O_2CH)_3$ (Lopez *et al*., 2006).

3.3 Characterization of E-wastes Using SEM

The surface morphology of the e-waste components was analysed using scanning electron microscopy (SEM). On the basis of the obtained results, SEM demonstrated noticeable morphological differences among the analysed samples. The micrographs in Figures 2 (a) to 2 (c) showed that the sample materials displayed porous and heterogeneous particle size distribution with sharp edges (except Figure 2 d) which shows blunt edges. In addition, the SEM micrographs showed particles which have brighter shades of grey (Figures 2 b, c and f). This brightness could be as a result of the interaction of the samples with electron beam (Silva *et al*., 2019).

The surface morphology also showed smaller particle sizes as well as larger particle sizes of 20 µm. The variable sizes and shapes of the aggregate crystallites having oval shape which form into clusters indicate non-uniformity and porosity of the analysed samples. They are in fact, polycrystalline in nature. The particles with small sizes could provide larger surface areas. The morphology of these minerals was similar to those reported in literature (Silva *et al*., 2019; Konne and Christopher, 2017).

3.4 Characterization of E-wastes Using FTIR

The FTIR was employed to elucidate the functional groups as displayed in the infrared spectrum of the sample to indicate the components of the sample containing the various functional groups and to determine the finger prints of infra-red bands related to the recovered mineral phases. The FTIR spectrum of the pure extracts obtained from e-waste sample A (IC) as displayed in Figure 3 (a) is a plot of intensity against wavelength. The highest peak with an intensity of 96.70 is observed at a wavelength of 2087 cm^{-1}. In the analysed e-waste samples A to J, the highest peak indicates the characteristic functional group present in the samples. In sample A, the peak at 2087 $cm^{-1}$is ascribed to the stretching vibration of C-N bond of the alkylnitriles. The band at 3384 cm^{-1} corresponds with the FTIR band of halite.

The FTIR spectrum of e-waste sample B (Aluminium cover) (Figure 3 b) showed the highest peak with an intensity of 89.65 at a wavelength of 2117 cm^{-1}. The highest peak is also ascribed to the stretching vibration of C-N bond of the alkylnitriles or cyano group.

For sample C (Condenser), the highest peak with an intensity of 93.12 is observed at a wavelength of 2974 cm^{-1} (Figure 3 c). The highest peak is ascribed to the stretching vibration of C-H bond of the alkane. Its finger print region at 1021 cm^{-1} showed the presence of vallerite. Additionally, the peak with an intensity of 77.21 observed at a wavelength of 3429 cm^{-1} is ascribed to the stretching vibration of O-H bond of the primary alcohol.

Sample D (Capacitor) (Figure 3 d) had the highest peak with an intensity of 92.18 at a wavelength of 2117 cm^{-1}. The highest peak is ascribed to the stretching vibration of C-N bond of the alkylnitriles or cyano group with a finger print region of 1638 cm^{-1} showing the presence of magnetite

The FTIR spectrum of e-waste sample E (Chopper transformer) as displayed in Figure 3 (e) had the highest peak with an intensity of 75.82 observed at a wavelength of 3377 cm^{-1}. The highest peak is ascribed to the stretching vibration of N-H bond of the primary amines. The finger print region that corresponds with thenardite was 1364 cm^{-1}.

Figure 3 (f) showed the FTIR spectrum of sample F (Transistor) with the highest peak of intensity (94.59) observed at a wavelength of 2117 cm^{-1}. The highest peak is ascribed to the stretching vibration of C-N bond of alkylnitriles. The peak at 1467 cm^{-1} is an indication of calcium hydroxide.

Figure 3 (g) showed the FTIR spectrum of sample G (Battery) with the highest peak of intensity (95.13) observed at a wavelength of 2095 cm^{-1}. The highest peak is ascribed to the stretching vibration of C-N bond of alkylnitriles. Its finger print region at 640 cm^{-1} showed that it is chalcopyrite.

Sample H (PCB) (Figure 3 h) had the highest peak with an intensity of 96.67 at a wavelength of 1401cm^{-1}. The highest peak is ascribed to the stretching vibration of NO_2 or NO bond of the

aromatic nitro group. The peak at 1014 cm^{-1} showed the presence of gibbsite. For sample I (Diode), the highest peak with an intensity of 89.59 is observed at a wavelength of 2117 cm^{-1} (Figure 3 i). The highest peak is ascribed to the stretching vibration of C-N bond of alkylnitrile. The peak at 1349 cm^{-1} is the finger region of sylvine sodian. Sample J (Resistor) (Figure 3 j) had the highest peak with an intensity of 93.94 at a wavelength of 1998 cm^{-1}. The highest peak is ascribed to the stretching vibration of C-O bond of the keto group. The peak at 3362 cm^{-1} showed the presence of gibbsite.

3.5 Composition of Metal Oxides in Raw and Recovered E-wastes

The EDXRF analysis for composition of metal oxides in e-waste for raw sample A (IC) showed SnO_2 (5.30 %) as the highest metal oxide present as displayed in Figure 4 (a). The non-metal oxides such as SiO_2 (80.17 %) and Sb_2O_3 (56.51 %) are the highest non-metal oxides present in raw sample A (Figure 4 (a)). This is an indication that raw sample A consists mainly of metallic and non-metallic oxides with accompanying transition metal oxides such as Fe_2O_3, CuO and PbO as impurities. The high percentage of SiO_2 (a non-metallic oxide) in the sample could be attributed to silicon (Si) being in the same group IV in the periodic table of elements with tin (Sn). This is in agreement with the XRD analysis result for raw sample A where quartz (SiO_2) was the only mineral phase in the sample. The recovered sample A had Al_2O_3 (10.85 %) as the highest metal oxide and SnO_2 (5.70 %) as the highest non-metal oxide with traces of chlorine, Cl, (6.46 %) and other transition metal oxides, non-metal oxides and metal oxides as impurities. Thus, the recovered sample A has a corundum structure as Al_2O_3 is a higher or complex oxide. The XRD analysis result for recovered sample A identified Halite (NaCl) as the major mineral phase. The presence of Cl in the recovered sample is an indication that the major mineral phase (Halite) could actually be tin halide ($SnCl_2$) with Fe, Zn and Pb halides as impurities. The EDXRF analysis for raw and recovered samples is a plot of counts against voltage (KeV). For raw and recovered sample A, the highest peak showed Sn as the major element with Fe, Zn and Pb as minor elements (peaks). This implies that e-waste samples comprise of various or heterogeneous (alloying) metals. The raw sample A could be an alloy of bronze (particularly coinage bronze or common bronze) used in valves, wires and utensils. The recovered sample A could be of the gum-metal bronze which has the property of hardness, toughness and capable of withstanding high pressures. It contains Fe as impurities.

The e-waste raw sample B (Aluminium Cover) had Al_2O_3 (27.87 %) as the major metal oxide with minor traces of MgO, SiO_2 and SnO_2 as impurities while the recovered sample B had Fe_2O_3 (26.96 %) as the major metal oxide with Cl (12.57 %) and traces of metal oxides like Al_2O_3 and SnO_2 as impurities (Figure 4 b). Thus, recovered sample B could contain Fe oxides and Fe chlorides with traces of Al. Therefore, raw and recovered sample B could be of the corundum formation. However, the presence of Cl in recovered sample B could be an indication of the presence of $FeCl_3$ in the sample. The conducted XRD analysis for raw sample B confirmed Aluminium as the major mineral structure. The EDXRF analysis for raw sample B showed Zn as the major element while the recovered sample showed Fe as the major element present. Raw sample B is a Zn metal mixed with Fe and Pb while the recovered sample B is a ferrous alloy.

In Figure 4 (c), raw sample C (Condenser) showed Al_2O_3 (14.22 %) as the major metal oxide alongside monoxides such as ZnO, MgO, CaO and mixed oxides such as Fe_2O_3 and SnO_2 as

impurities. The high value of Al_2O_3 indicated that sample C is an alloy of duralumin (Al, Cu, Mn, Mg), which is a good conductor of heat and electricity. Raw sample C also contained SiO_2 (19.62 %) as the only non-metallic oxide. The recovered sample C showed CuO (66.89 %) as the highest metal oxide obtained with traces of Co_3O_4 (5.57 %) and SnO_2 (1.00 %). However, the EDXRF analysis for raw sample C indicated Zn while the recovered sample C indicated Cu as the major element found. Hence, it could contain Cu alloy (based on the principal metal in the alloy). The EDXRF elemental composition and analysis results for recovered sample C confirmed the XRD patterns showing CuO/Cu compounds.

For raw and recovered samples D (Capacitor), CaO appeared in the two samples (23.41 % and 17.39 %) respectively as the major metal oxides obtained. Raw sample D also comprise of other transition and metal oxides such as Fe_2O_3, ZnO, MgO, Al_2O_3 and SnO_2 as well as non-metal oxides like SiO_2 and Sb_2O_3. Recovered sample D also contained some quantities of metal and non-metal oxides such as Fe_2O_3, CuO, Al_2O_3, SnO_2, MnO, SiO_2 and traces of Cl as impurities (Figure 4 d). It also showed Mn, Fe and traces of Zn. In the EDXRF analysis, Zn showed the highest peak for raw sample and Fe for recovered sample. Raw sample D is a mixture of Zn metal with Fe and Pb while the recovered sample is a mixture of Fe and Mn with traces of Zn.

The raw sample E (Chopper Transformer) showed the major metal oxide as CuO (52.47 %) with accompanying metal oxides such as Fe_2O_3, MgO, CaO, and SnO_2, and non-metal oxides such as SiO_2 and Sb_2O_3 as impurities while the recovered sample showed Co_3O_4 (26.70 %) with impurities such as Fe_2O_3, CuO and SnO_2 (Figure 4 e). Coincidentally, the EDXRF analysis for raw sample E showed Cu while the recovered sample showed Co as the metals with highest peaks. Therefore, recovered sample E contained cobalt oxide with Na_2SO_4 and CuO traces. With the high presence of Co_3O_4 (26.70 %), recovered sample E could be described as the sample having a spinel formation. Raw sample E could be an alloy of bronze.

In the case of raw sample F (Transistor), the major metal oxide obtained was Fe_2O_3 (14.31 %) with other transition and metal oxides such as CuO, MgO, Al_2O_3, CaO, SnO_2 and PbO as impurities. Raw sample F also has a high percentage of SiO_2 (49.87 %) (Figure 4 f). The recovered sample F showed Co_3O_4 (45.77 %) as the major metal oxides with impurities like CuO, Al_2O_3, and SnO_2 (Figure 4 f). On the basis of the EDXRF analysis for raw sample F, Fe was obtained while for the recovered; Co was obtained as the prominent metal. Therefore, the high presence of higher oxides like Fe_2O_3 and Co_3O_4 in both raw and recovered sample F respectively could be attributed to sample F having a corundum structure and a spinel structure respectively. However, raw sample F is a ferrous alloy. It could be brass alloy since it contains Cu and Zn, though as impurities. More so, since the colour of Cu is red/brown and Zn is silver-white, an alloy of these (Cu + Zn) is brass which is yellow in colour. It is used as brass musical instruments.

Figure 4 (g) showed Co_3O_4 (56.37 %) as the major metal oxide for raw sample G (Battery) and Fe_2O_3 (10.39%) as the major metal oxide for recovered sample G with accompanying metal and non-metal oxides like CuO, Al_2O_3, SiO_2, SnO_2, P_2O_5 and Al_2O_3, SnO_2, Co_3O_4 respectively. Similarly, the EDXRF analysis showed Co for raw sample G and Fe for recovered sample G as the major metals with highest peaks. The recovered sample G could possibly contain the chlorides of Fe with traces of Al and Co. On the basis of the analysed results, raw sample G could be adjudged to be of the spinel formation which crystallizes in the cubic system and the recovered

sample to be of the corundum structure which crystallizes in the trigonal system and occurs as well-developed hexagonal crystals. The high concentration of Co_3O_4 in the raw sample could likely be due to its presence in the chemical composition of battery powder (Urbanska, 2020). The recovered sample could be Alnico alloy, used as magnets in loudspeakers and pickups in electric quitars.

The EDXRF elemental composition for raw sample H (PCB) had SnO_2 (11.44 %) as the major transition metal oxide with accompanying metal and transition metal oxides (Fe_2O_3, CuO, MgO, Al_2O_3, CaO, PbO, MnO, Co_3O_4, CdO, Rb_2O and non-metal oxides (, SiO_2, Sb_2O_3, P_2O_5) including Br and Cl (Figure 4 h). The recovered sample H showed Al_2O_3 (63.67 %) as the major metal oxide with traces of Fe_2O_3, CuO, MgO, SnO_2, and, SiO_2 as impurities (Figure 4 h). Meanwhile, the EDXRF analysis result for the raw sample H had Sn as the element with highest peak with Pb, Cu, Fe, Zn and Co as minor peaks, and it is a solder alloy (particularly brazing alloy) used for soldering steel joints by fussion process. The recovered sample H, recorded Cu as the major element with traces of Fe, Sn, Zn, Cu, K and Pb as impurities, and it is a bronze (gun-metal) with the presence of Cu, Sn and Zn (impurities). Copper was also discovered as the most abundant metal in e-waste that represents up to 20 % by weight of PCBs (Baniasadi *et al*., 2020). Accordingly, the XRD patterns showed 100 % Cassiterite (SnO_2) and 84.1 % Gibbsite Al $(OH)_3$) as the mineral phases. However, Ajiboye *et al*., (2019) reported the presence of SnO_2 and CuO as the main oxides present in the PCB with other minor oxides as ZnO, PbO, $ZnSiO_3$, Cu Fe_2O_4 , Ni (TiO_3) and Fe_2O_3.

The major metal oxide present in raw sample I (Diode) was Co_3O_4 (7.74 %). There is also the high percentage of non-metallic oxides like SiO_2 (38.28 %) and Sb_2O_3 (29.02 %) with accompanying metal and transition metal oxides such as Fe_2O_3, CuO, MgO, Al_2O_3, CaO, SnO_2, PbO, Rb_2O and CdO as impurities (Figure 4 i). In the recovered sample I, MgO (4.92 %) with CuO (3.41 %) were observed with MgO as the major metal oxide. However, there are traces of impure oxides such as Al_2O_3, CaO, SnO_2, and SiO_2. In the EDXRF analysis, Sn and Cu had the highest peaks for raw and recovered samples respectively. There are traces of Fe, Pb, Cu and Co as impurities for the raw sample and Cu, Fe and Ca as impurities for the recovered sample I. Hence, raw sample I is of the bronze alloy.

The EDXRF elemental composition for raw sample J (Resistor) recorded Fe_2O_3.
(17.12 %) as the major metal oxides while the recovered sample J recorded Al_2O_3 (29.68 %) as the major metal oxide with a close metal oxide, CuO (25.55 %) (Figure 4 j). The raw sample J also had SiO_2 (47.66 %) as the major non-metal oxide present with other oxides such as CuO, MgO, Al_2O_3, CaO, SnO_2, PbO, TiO_2, Co_3O_4 and CdO as impurities. The recovered sample J had Fe_2O_3, SnO_2, Sb_2O_3 and Cl as impurities. The EDXRF analysis for raw sample J however, recorded Fe as the major metal (element) (with highest peak) while the recovered sample recorded Cu as the major element with traces of Cu and Fe impurities shown on the XRF result. Raw sample J could be a ferrous alloy mixed with Babbitt metal (Sn and Cu).

4.0 Conclusion

The mineralogical characteristics of both raw and recovered e-waste samples using XRD revealed the predominant mineral phases such as quartz, alumina, alumina, calcite, quartz, quartz, quartz, cassiterite, quartz and quartz for raw samples A to J respectively as well as halite, vallerite, manganite, thenardite, calcium hydroxide, chalcopyrite, gibbsite, sylvine sodian and gibbsite for

recovered samples A and C to J respectively. The results of the SEM analysis indicated noticeable morphological differences among the samples. FTIR identified the functional groups and infrared bands related to the recovered mineral phases contained in the e-waste samples analysed. However, EDXRF confirmed the presence of metal oxides in percentages in the raw and recovered e-waste samples and also the predominant elements in each of the samples. Some metal oxides that were found in the raw components were found to be absent or non-crystalline in the recovered compounds The characterization of e-waste components should be conducted in order to reveal the correlation between toxic substances in e-waste and recovery (treatment) strategies.

Acknowledgment

The authors acknowledged Tertiary Education Fund (TETFund) Kenule Beeson Saro-Wiwa Polytechnic, Bori, Rivers State, Nigeria for their sponsorship.

References

Abalansa, S., Mahrad, B. E., Icely, J. and Newton, A. (2021). Electronic Waste, An Environmental Problem Exported to Developing Countries: The Good, The Bad and The Ugly, *Sustainability*, 13: 1-24.

Agbaei, M., Imani, M. and Tadjarodi, A. (2020). Preparation of Cu4SnS4/$CuCo_2S_4$ Nanaparticles Using Combustion Reaction Accelerated by Organic Driving Agents under Microwave Irradiation, *Chemistry Proceedings Presented at the 24th International Electronic Conference on Synthetic Organic Chemistry*, 15th November-15th December, 2020; Available Online: https;//ecsoc-24.sciforum.net/.

Ajiboye, A. E, Olasehinde, F. E, Adebayo, O. A, Ajayi, O. J, Ghosh,,M. K and Basu,, S. (2019). Extraction of Copper and Zinc from Waste Printed Circuit Boards, *Recycling*, 4, 36, 1-13.

Alzate, A., Lopez, M. E., Serna, C. and Gonzalez, O. (2016). Gold Recovery from Electronic Waste by Pressure Oxidation. *Proceedings of the 2nd World Congress on Mechanical, Chemical and Material Engineering (MCM'16) Budapest, Hungary*, August 22nd-23rd, 2016.

Antao, S. M., Hassan, I. Wang, J. Lee, P. L. and Toby, B. H. (2008). State-of-the-art High-Resolution Powder X-ray Diffraction (HRPXRD) illustrated with Rietveld Structure Refinement of Quartz, Sodalite, Tremolite, and Meionite, *The Canadian Mineralogist*, 48 (6),1501-1509.

Arslan, Y., Kenduzler, E., Adiguzel, V. T. and Tomul, F. (2019). The Effect of Synthesis Conditions on Calcium Silicate, *Bioceramic Materials, Suleyman Demirel University Journal of Natural and Applied Sciences*, 23 (3), 727-737.

Ashok, C., Rao, K. V. and Chakra, C. S. (2014). Structural Analysis of CuO Nanomaterials Prepared by Novel Microwave Assisted Method, *Journal of Atoms and Molecules*, 4 (5), 803-806.

Baniasadi, M., Graves, J. E., Ray, D. A., De Silva, A. L., Renshaw, D. and Farnaud, S. (2020). Closed-Loop Recycling of Copper from Waste Printed Circuit Boards Using Bio-leaching and Electro-winning Processes. *Waste and Bio-mass Valorization, (In-press). Available online: https://dx.doi.org/10.1007/s12649-020-01128-9 (accessed on 5th September, 2020).*

Beaulieu, L. Y., Beattie, S. D., Hatchrd, T. and Dahn, J. R. (2003). The electrochemical reaction of Lithium with Tin Studied by In Situ AFM, *Journal of the Electrochemical Society*, 150 (4), 266-270.

Borthakur, A. (2016). International Perspectives/Special Report: Health and Environmental Hazards of Electronic Waste in India. *Journal of Environmental Health*, 78: 18- 23.

Davis, G. and Heart, S. (2008). Electronic Waste: The Local Government Perspective in Queensland, Australia. *Resources, Conservation and Recycling*, 52, 1031-1039.

Debnath, B., Roychowdhury, P. and Kundu, R. (2016). Electronic Components Reuse and Recycling. A New Approach towards WEEE Management. *Procedia Environmental Sciences*, 35, 656-668.

Deng, X., Chen, R., Zhuo, S. Zhou, G.and Shi, Y. (2019). Bioleaching Characteristics of Heavy Metals from Polluted Soil with Indigenous *Aspergillus niger* F2, *Journal of Biobased Materials and Bioenergy*, 13 (30), 401-409.

Ewuim, S. C., Akunne, C.E., Abajue, M. C., Nwankwo, E. N. and Faniran, O. J. (2014). Challenges of E-waste Pollution to Soil Environments in Nigeria – A Review. *Animal Research International*, 11 (2), 1976-1981.

Feng-Hua, C., Chang-Wei, G., Yan-Ping, G., Min-Gang, Z. and Yue-Sheng, C. (2014). Martensitic Transformation and Giant Magnetic Entropy Change in $Ni_{42.8}Mn_{40.3}Co_{5.7}Sn_{11.2}$ Alloy, *Chinese Physics B*, 23 (6), 1-6.

Gao, T. and Liu, X. (2017). Morphological Evolution and Strengthening Behaviour of α-Al (Fe, Mn) Si in Al-6Si-2Fe-xMn Alloys. *Results in Physics*, 7, 1051-1054.

Gogebakan, M., Avar, B. and Uzun, O. (2009). Quasicrystalline Phase Formation in the Conventionally Solidified Al-Cu-Fe System, *Materials Science-Poland*, 27 (3), 919-926.

Gu, Y., Wu, Y., Xu, M., Mu, X. and Zuo, T. (2016). Waste Electrical and Electronic Equipment (WEEE) Recycling for a Sustainable Resource Supply in the Electronics Industry in China. *J. Clean. Prod*., 127, 331-338.

Guan, M., Hu, Y., Zheng, T., Zhao, T. and Pan, F. (2018). Composition, Optimization and Mechanical Properties of Mg-Al-Sn-Mn Alloys by Orthogonal Design, *Materials*, 11, 1424, 1-17.

Hiraga, R., Gomes, O. D. F. M., and Neumann, R. (2021). Maghemite in Brazilian Iron Ores: Quantification of the Magnetite-Maghemite Isomorphic Series by X-ray Diffraction and the Rietveld Method, and Confirmation by Independent Methods, Minerals, 11, (346), 1-19.

Hou, J., Luo, W., Luo, S., Lin, C., Liu, P., Liao, X., Jing, F. and Li, X. (2017). Facile Synthesis of CuMAI (M=G, Mn, Zn and Co) with Highly Dispersed Cu and Tailorable Surface Acidity for Efficient 2-Methylpyrazine Synthesis. *Royal Society of Chemistry Advances*, 7, 48662-48669.

Isildar, A., Hullebusch, E. D. V., Lenz, M., Laing, G. D., Marra, A., Cesaro, A., Panda, S., Akcil, A., Kucuker, M. A. and Kuchta, K. (2019). Biotechnological Strategies for the Recovery of Valuable and Critical Raw Materials from Waste Electrical and Electronic Equipment (WEEE)-A Review. *Journal of Hazardous Materials*, 362: 467-481.

John, C. F., Paul, R. C., Singh, S. C. E., Jacobjose, J., Ramkumar, T., Hikku, G. S. , Sharma, R. K. and Sengottuvel, P. (2018). Corrosion Behaviour of ZrC Particles Reinforcement with Al-12Si Composites by Weight Loss Method using Acidic Media, *Bulletin of the Polish Academy of Sciences, Technical Sciences*, 66 (1), 1-16.

Karipoth, P., Thirumurugan, A., Velaga, S., Creneche, J. and Joseyphus, R. J. (2016). Magnetic Properties of FeCo Alloy Nanoparticles Synthesized through Instant Chemical Reduction, *Journal of Applied Physics*, 120 (12), 123906.

Kaur, K. and Pandey, O. P. (2013). High Temperature Sliding Wear of Spray-Formed Solid-Lubricated Aluminum Matrix Composites, *Journal of Materials Engineering and Performance*, 22, 3101-3110.

Khaliq, A., Rhamdhani, M. A., Brooks, G. and Massod, S. (2014). Metal Extraction Australian Perspective. *Resources*, 3, 152-179.

Kim, Y., Seo, H. and Roh, Y. (2018). Metal Recovery from the Mobile Phone Waste by Chemical and Biological Treatments. *Minerals*, 8 (8), 1-10.

Kolencik, M., Urik, M., Cernansky, S., Molnarova, M. and Matus, P. (2013). Leaching of Zinc, Cadmium, Lead and Copper from Electronic Scrap Using Organic Acids and the *Aspergillus Niger* Strain. *Fresenius Environmental Bulletin*, 22 (120), 3673-3679.

Konne,J. L. and Christopher, B. O. (2017). Sol-Gel Syntheses of Zinc Oxide and Hydrogenated Zinc Oxide (ZnO:H) Phasas, Hindawi Journal of Nanotechnology, 1-8. http://doi.org/10.1155/2017/5219850.

Mishra, B. and Lee, H. (2018). Selective Recovery and Separation of Copper and Iron from Fine Materials of Electronic Waste Processing. *Mineral Engineering, 123:1-7.*

Lopez, S .Y. R., Rodriguez, J. S. and Sueyoshi, S. S. (2006). Low Temperature Formation of Alpha Alumina Powders via Metal Organic Synthesis, *The Azo Journal of Materials Online*, 2, 1-6.

Lopez-Juarez, R., Razo-Perez, N., Perez-Juache, T. J., Hernandez-Cristobal, O. and Reyes-Lopez, S. Y. (2018). Synthesis of α-Al_2O_3 from Aluminum Cans by Wet-Chemical Methods, *Results in Physics*, 11, 1075-1079.

Madheshiya, A., Kumar, S. and Gautam, C. R. (2017). Synthesis, Structural and X-ray Absorption Spectroscopy of (PbxxBi1-x), TiO3 Borosilicate Glass and Glass Ceramics, *Journal of Asian Ceramic Societies*, 248, 1-9.

Magalini, F. U., Kuehr, R. U. and Balde, C. P. U. (2015). E-waste in Latin America; United Nations University, Tokyo, Japan, pp.37.

Nilchi, A., Dehaghan, T. S. and Garmarodi, S. R. (2013). Kinetics, Isotherm and Thermodynamics for Uranium and Thorium Ions Adsorption from Aqueos Solutions by Crystalline Tin Oxide Nanoparticles, *Desalination*, 321, 67-71.

Nyamjargal, L., Batdemberel, G., Burmaa, G. and Burmaa, D. (2018). Effect of Roasting Temperature for Copper Leaching of Sulfide Concentrate by Combined Methods. *Open Journal of Applied Sciences*, 8, 545-553.

Ongondo, F. O., Williams, I. D. and Cherrett, T. J. (2011). How is WEEE doing? A Global Review of the Management of Electrical and Electronic Wastes, *Waste Manag*., 31: 714-730.

Padil, V. V. T. and Cernik, M. (2013). Green Synthesis of Copper Oxide Nanoparticles Using Gum Karaya as a Biotemplate and their Antibacterial Application, *International Journal of Nanomedicine*, 8 (1), 889-898.

Pang, X., Tan, C. Dai, X. and Zhang, S. (2014). Performance Enhancement of Sn-Sb-Co Alloy Film Anode for Lithium-Ion Batteries via Post Electrodissolution Treatment, *Journal of Applied Electrochemistry*, 45 (2), 115-122.

Pant, D., Joshi, D., Upreti, M. K.. and Kotnata, R.K. (2012). Chemical and Biological Extraction of Metals Present in E-waste: A Hybrid Technology, *Waste Manag*ement, 32 (5): 979-990.

Qi, N., Hu, M., Wang, Z., Lu, Z. and Xie, C. (2013). Synthesis of Al/Fe_3Al Core-Shell Intermetallic Nanoparticles by Chemical Liquid Deposition Method. *Advanced Powder Technology*, 24, 926-931.

Raja, P. B., Nasir, M. and Ibrahim, M. (2022). Characterisation of Nanomaterial used in Nano-bioremediation, *NanoBioremediation: Fundamentals and Applications*, 57-83.

Robinson, B. H. (2009). E-waste: An Assessment of Global Production and Environmental Impacts. *Sci. Total Environ*, 408: 183-191.

Sahan, M. Kucuker, M.A., Demirel, B., Kuchta, K. and Hursthouse, A. (2019). Determination of Metal Content of Waste Mobile Phones and Estimation of their Recovery Potential in Turkey. *International Journal of Environmental Research and Public Health*, 16 (5), 887.

Silva, T. H., Castro, A. C. M., Neto, F. C. V., Soares, M. M. N. S., Resende, D. S., Bezerra, A. C. S. (2019). Recycling Ceramic Waste as a Raw Material in Sanitary Ware Production, *Ceramica*, 65, 426-431.

Tran, B. H., Tieu, K., Wan, S., Zhu, H., Cui, S. and Wang, L. (2018). Understanding the Tribological Impacts of Alkali Element on Lubrication of Binary Borate Melt. *Royal Society of Chemistry Advances*, 8, 28847-28860.

Urbanska, W. (2020). Recovery of Co, Li, and Ni from Spent Li-loin Batteries by the Inorganic and/ or Organic Reducer Assisted Leaching Method. *Minerals*, 10 (6), 555, 1-13.

Wang, Z., Zhang, B. and Guan, D. (2016). Take Responsibility for Electronic-waste Disposal. *Nature*, 536 (7614), 23-25.

Xu, Y., Ding, D., Yang, X., Zhang, W., Gao, Y., Wu, Z., Chen, G., Chen, R., Huang, Y. and Tang, J. (2019). Effect of Si Addition on Mechanical and Electrochemical Properties of Al-Fe-Cu-La Alloy for Current Collector of Lithium Battery. *Metals*, 9 (1072), 1-14.

Yamane, L. H., De-Moraes, V. T., Espinosa, D. C. R. and Tenorio, J. A. S. (2011). Recycling of WEEE: Characterisation of Spent Printed Circuit Boards from Mobile Phones and Computers. *Waste Management*., 31, 2553-2558.

Yunus, P. A. and Sengupta, B. (2016). E-waste Indian Perspective and Recovery of Valuable Metals from E-waste−A Review. *International Refereed Journal of Engineering and Science*, 5(4): 70-80.

Zavasnik, J., Radmilovic, N., Arshad, M. S. and Recnik, A. (2014). Sonochemical Synthesis of Mackinawite and the Role of Cu Addition on Phase Transformations in the Fe-S System. *Journal of Nanoparticles Research*, 16 (2223), 1-13

Zhang, N., Bu, J., Meng, Y., Wan, J., Yuan, L. and Peng, X. (2020). Degradation of p-aminophenol Wastewater using Ti-Si-Sn-Sb/GAC Particle Electrodes in a Three-dimensional Electrochemical Oxidation Reactor: Degradation PAP by Three-dimensional Electrochemical Oxidation, *Applied Organometallic Chemistry*, 34 (6), e5612.

Zhao, Q., Li, X., Wu, Q., Liu, Y. and Lyu, Y. (2020). Evolution of Mineral Phases and Microstructure of High Efficiency Si-Ca-K-Mg Fertilizer Prepared by Water-Insoluble K-feldspar, *Journal of Sol-Gel Science and Technology*, 94 (1), 3-10.